MASTHING: a process-based model of mast seeding in European beech

Simone Bregaglio[1,*], Sofia Bajocco[1], Carlotta Ferrara[2], Michał Bogdziewicz[3], Andrew Hacket-Pain[4], Francesco Chianucci[2]

[1] Council for Agricultural Research and Economics (CREA) – GeoModel lab – Research Centre for Agriculture and Environment, Italy.

[2] Council for Agricultural Research and Economics (CREA) – Research Centre for Forestry and Wood, Italy.

[3] Forest Biology Centre, Institute of Environmental Biology, Faculty of Biology, Adam Mickiewicz University, Uniwersytetu Poznańskiego 6, 61-614 Poznań, Poland.

[4] Department of Geography and Planning, School of Environmental Sciences, University of Liverpool, Liverpool, United Kingdom.

*corresponding author: simoneugomaria.bregaglio@crea.gov.it

Abstract

Masting, the synchronised interannual variation in seed production, shapes forest regeneration and many ecosystem processes, yet process-based models remain underdeveloped. Here we introduce MASTHING (MASting THeory modellING), an individual-tree model coupling phenology, carbon gain, resource storage, temperature cues, and environmental vetoes on reproduction. We parameterised MASTHING for European beech (*Fagus sylvatica* L.) using 43 years of data from 97 trees across 11 sites in England, testing three variants: i) resource budget only, and extensions with ii) additive and iii) interactive temperature cue effects. The results reveal that the critical variable is not whether weather cues are incorporated, but how they are coupled to internal resource dynamics: the additive formulation (RB+WC) reproduced the observed interannual variability but degraded temporal performance relative to RB alone, whereas the interactive formulation (RB×WC) in which cue sensitivity is gated by resource status improved overall performance and classification skill (R^2 = 0.82). RB×WC provided the lowest forecast error at country calibration level (RMSE = 0.27), demonstrating structural robustness when parameterisation cannot be tailored to local conditions, while simpler formulations remained competitive for point-forecast accuracy at finer calibration scales. The model reproduced the long-term decline in masting intensity under climate warming (R^2 = 0.81). For four years of data excluded from model calibration, the model correctly identified the 2024 low-production event across multiple sites, though the 2025 crop was systematically overestimated, pointing to insufficient carry-over depletion after consecutive poor seed years as the main structural limitation. MASTHING provides a platform for testing masting hypotheses, evaluating climate change impacts, and supporting operational seed forecasting.

Keywords: climate change, masting, fecundity, forest resilience, tree demography

1. Introduction

Masting, the synchronized interannual variability in seed production among individuals within a population, is a common reproductive strategy in long-lived plants (Kelly & Sork, 2002; Journé *et al.*, 2023a). This variable reproduction enhances reproductive efficiency by reducing seed predation and improving pollination success (Kelly *et al.*, 2001; Rapp *et al.*, 2013; Zwolak *et al.*, 2022). The resulting boom-and-bust dynamics in seed supply have far-reaching implications for food webs, nutrient cycling, and the dynamics of plant and fungal communities, as well as for forest ecosystems and game management (Bisi *et al.*, 2018; Clark *et al.*, 2019; Pearse *et al.*, 2021; Tattoni *et al.*, 2025; Ostfeld *et al.*, 2026). Understanding the mechanisms underlying masting is therefore essential for predicting changes in plant populations and ecosystem functioning (Hacket-Pain & Bogdziewicz, 2021) and for providing short-term forecasts of seed production to support decision-making (Elliott & Kemp, 2016; Journé *et al.*, 2023b). These needs are becoming particularly urgent as climate change alters masting patterns, with large consequences for seed availability (Bogdziewicz *et al.*, 2023; Jantzen *et al.*, 2026). At the same time, demand for reliable short-term forecasting is increasing as seed supply for ecological restoration becomes a policy priority (Pearse *et al.*, 2021; Journé *et al.*, 2023b; Oberklammer *et al.*, 2026). For example, the European Union's Biodiversity Strategy for 2030 and the proposed EU Nature Restoration Law emphasise large-scale ecosystem restoration, which requires a dependable supply of seeds. Accurate forecasting is therefore essential to ensure adequate seed availability for restoration projects.

Building on this growing interest, recent decades have brought significant progress in understanding the processes driving interannual variation and synchrony in seed production (Crone & Rapp, 2014; Pearse *et al.*, 2016; Bogdziewicz *et al.*, 2024; Satake & Journé, 2026). These advances open the way to models capable of reproducing masting dynamics, enabling near-term forecasting and assessing climate change impacts on plant reproduction. However, most existing approaches remain primarily statistical (Journé *et al.*, 2023b; Wion *et al.*, 2025; Hirsch *et al.*, 2025; Oberklammer *et al.*, 2026). Process-based models offer an alternative, as they explicitly represent underlying biophysical mechanisms rather than relying on empirical relationships (Asse *et al.*, 2020; Mäkelä *et al.*, 2000). This mechanistic foundation can improve predictive skills, especially under changing environmental conditions, making such models powerful tools for ecological forecasting and management (Briscoe *et al.*, 2023). Moreover, because masting operates over multiple years and is difficult to manipulate experimentally (Bogdziewicz *et al.*, 2020a), process-based models provide a means to test hypotheses and simulate scenarios that are otherwise impractical in field studies (Végh & Kato, 2024).

Various models have been developed to explain masting, including those based on resource budgets, weather cues, and resource-limited floral induction (Isagi *et al.*, 1997; Kelly *et al.*, 2013;

Monks *et al.*, 2016; Pearse *et al.*, 2016). Rather than acting independently, the General Model of Masting (Bogdziewicz *et al.*, 2024) suggests that these mechanisms jointly regulate the transition from flowering to fruiting, with their relative importance varying across species. Resource budget models propose that plants must accumulate sufficient resources before reproduction, often over multiple years (Isagi *et al.*, 1997; Crone & Rapp, 2014), and experimental flower removal confirms that reproduction depletes resources and limits subsequent flowering (Sala *et al.*, 2012; Roncé *et al.*, 2023). In parallel, weather cue models suggest that plants evolved hypersensitivity to environmental variability, triggering large seed crops under favourable conditions such as specific temperature regimes (Janzen, 1971; Kelly *et al.*, 2013; Fernández-Martínez *et al.*, 2017; Yeoh *et al.*, 2017; Bogdziewicz *et al.*, 2020b). Resource-limited floral induction links these mechanisms by proposing that responses to weather cues depend on internal resource status (Monks *et al.*, 2016; Kelly *et al.*, 2025). For example, in *Nothofagus solandri*, nitrogen fertilization removed resource limitation, resulting in a positive relationship between temperature during flower formation and seed production that was absent in non-fertilized control stands (Smaill *et al.*, 2011). Together, these advances provide a solid conceptual basis for process-based models of masting. However, such models remain rare (Vacchiano *et al.*, 2018), and recent developments still require evaluation under changing climatic conditions (Végh & Kato, 2024).

Here, we present MASTHING (MASting THeory modellING), a simulation model that represents key processes underlying plant growth and reproduction. The model proposes a resource budget framework coupled to plant phenology, where carbon gained through photosynthesis is allocated to reproduction as a function of internal resource status and environmental cues. We parameterised MASTHING for European beech (*Fagus sylvatica* L.) using 43 years of seed production data (1980–2022) from 97 trees across 11 sites in England (Packham *et al.*, 2008; Bogdziewicz *et al.*, 2020c). We compared three model formulations that differ in how environmental cues modulate reproductive allocation and evaluated their behaviour under three calibration strategies spanning individual-tree, site-level, and country-wide parameterisation. A sensitivity analysis was performed to identify the parameters that most strongly govern simulated reproductive dynamics. Using this framework, we tested whether the proximate mechanisms hypothesised to drive masting in beech can reproduce observed reproductive patterns and their recent breakdown under climate warming, characterised by reduced interannual variability and synchrony in seed production. This decline has been attributed to more frequent temperature cues, which shorten resource recovery intervals and dampen reproductive responses (Bogdziewicz *et al.*, 2021; Hacket-Pain *et al.*, 2025; Kelly *et al.*, 2025). MASTHING provides a mechanistic tool to evaluate these hypotheses under changing environmental conditions and to assess near-term forecasting skill (2023–2026).

2. Materials and Methods

2.1. Model description

MASTHING is a process-based simulation model of individual tree growth and reproduction derived from the resource-budget theory of Isagi *et al.* (1997). The model simulates reproductive investment and wood growth at a daily time step through a carbon partitioning scheme that couples the two processes and allows their interaction to propagate across successive years. Although the model is generic in its formulation, it has been parameterised here for European beech. A full mathematical description of all model components is given in Supplementary Material S1. MASTHING is implemented in C# as a class library coupled with a console application for execution, parameter optimisation, and sensitivity analysis, with code available in an open-access repository (Bregaglio et al., 2026; https://github.com/GeoModelLab/MASTHING, DOI: 10.5281/zenodo.19660460).

2.1.1. Overall model structure and carbon balance

MASTHING integrates four coupled modules: A) tree allometry, B) phenology, C) carbon balance, and D) reproductive allocation (Figure 1).

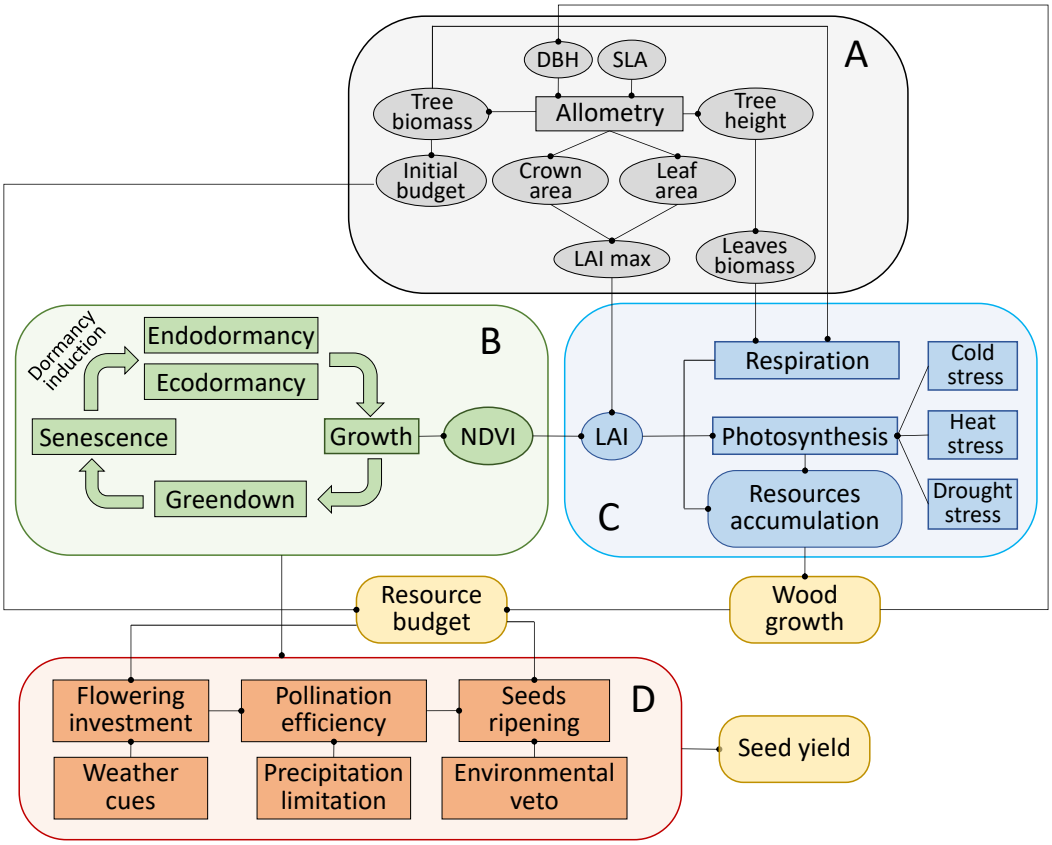

Figure 1. Conceptual diagram of the MASTHING model showing interlinked modules and simulated processes. (A) variables associated with the tree allometry module; (B) phenological processes; (C) processes related to resource accumulation; (D) reproductive allocation. Lines and nodes connections indicate relationships among variables and modules.

An individual tree is initialized from allometric relationships based on diameter at breast height (DBH, measured at 1.3 m), which are used to estimate crown projection area, tree height, and biomass partitioning among plant compartments (Figure 1A; Bartelink, 1997; Zianis & Mencuccini, 2004). Foliage biomass is converted into leaf area index using specific leaf area (SLA, m^2 kg^{-1}) scaled to crown projection area, yielding maximum leaf area index LAI_{max} (Figure 1A). Phenological dynamics are simulated using the SWELL model (Bajocco *et al.*, 2025), which describes the transition from dormancy to the growing season and the progression of key phenophases (Figure 1B). The resulting simulated Normalised Difference Vegetation Index (NDVI) is scaled over the growing season (bud burst to leaf fall) and used to derive daily leaf area index (LAI) by proportional scaling to LAI_{max} (Bregaglio *et al.*, 2023). Carbon assimilation is computed using a light-use efficiency framework (Figure 1C; Monteith, 1972; Medlyn, 1998). Gross primary production is estimated as the product of light use efficiency (LUE, g C MJ m^{-2}) and incident solar radiation, downregulated by heat, frost, and water stress functions (Zhao *et al.*, 2019; Maselli *et al.*, 2020). Maintenance respiration of woody and foliar tissues is represented using a temperature-dependent Q_{10} formulation (Lin *et al.*, 2012), with separate base rates for wood and leaf biomass. The daily net carbon balance determines the carbon available for allocation, which is partitioned between reproductive investment and wood growth. The fraction directed to wood growth is regulated dynamically by prior-year reproductive expenditure: higher reproductive investment in the previous year (Y−1) reduces the wood carbon allocation in the current year (Y), coupling growth and reproduction across successive years (Hacket-Pain *et al.*, 2025; Barczyk *et al.*, 2026). The accumulated net carbon pool constitutes the internal resource budget (B_t, g C m^{-2}), the central state variable governing annual reproductive potential (Figure 1D).

The maximum storage capacity (B_{max}, g C m^{-2}) is derived from tree allometry as a fraction of aboveground carbon biomass normalized to crown projection area and represents the effective upper bound on storable carbon. The resource budget B_t is normalized relative to a minimum reproduction threshold ($B_{min} = REP_{thr} \times B_{max}$) and the maximum storage capacity B_{max} to yield a dimensionless budget level ($BL_t \in [0, 1]$, Equation 1):

$$BL_t = (B_t - B_{min})/(B_{max} - B_{min}) \quad [1]$$

where $REP_{thr} \in [0, 1]$ is a reproduction threshold parameter defining the minimum budget fraction below which no reproductive investment occurs ($BL_t = 0$ when $B_t \leq B_{min}$; $BL_t = 1$ when $B_t = B_{max}$). Reproductive allocation (Figure 1D) links the internal resource budget to seed production through flowering investment, pollination, and seed maturation, all modulated by environmental conditions.

2.1.2. Reproductive allocation, temperature cues and environmental regulation

Reproductive investment is allocated sequentially to flowering and seed production (Figure 2). Flowering represents the initial carbon cost subtracted from the internal resource budget. The conversion of flowers into seeds depends on pollination success and carbon availability during seed ripening. Environmental conditions modulate reproductive outcomes at distinct stages of the growing season (Figure 2A).

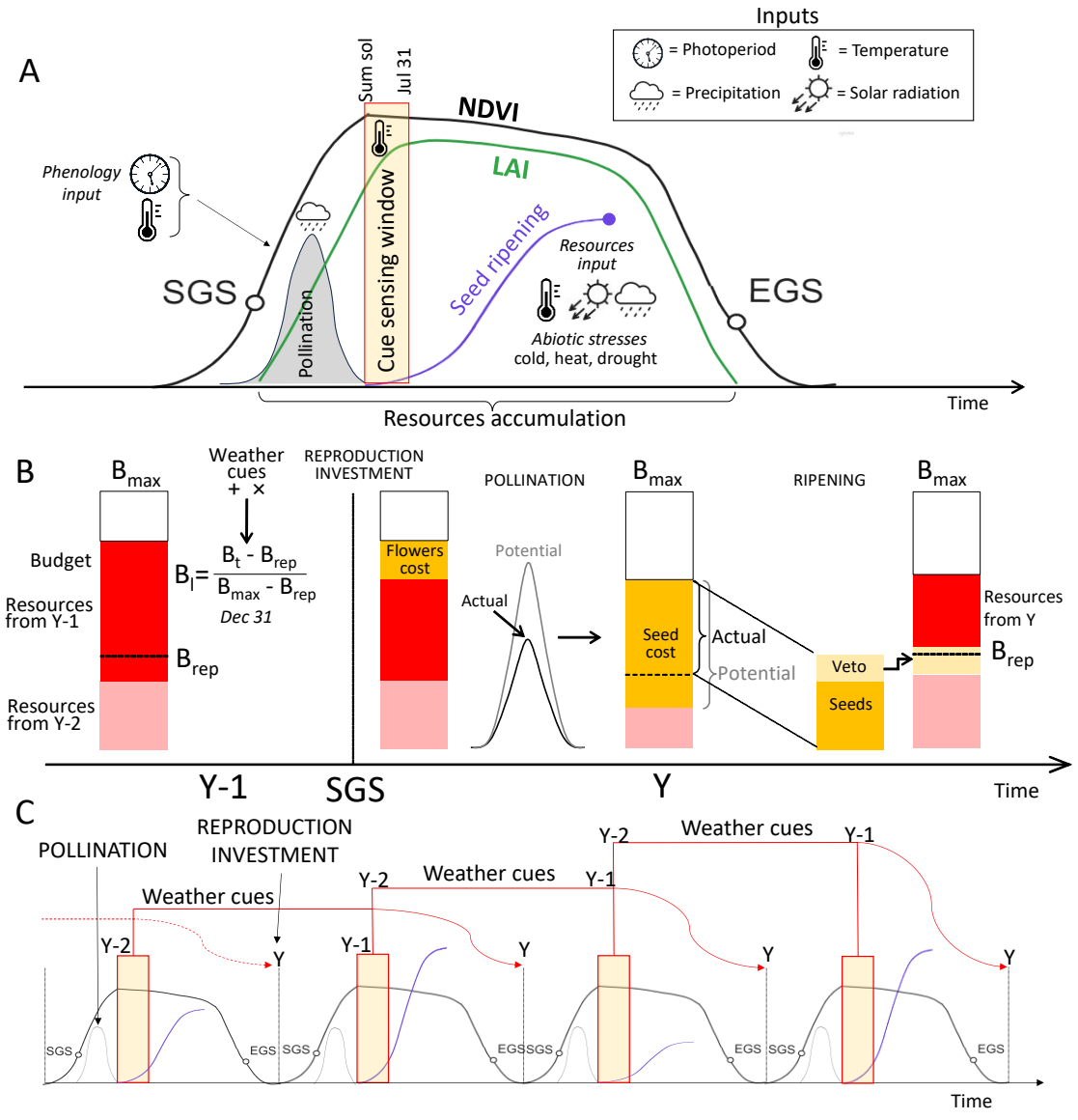

Figure 2. Overview of the MASTHING model across temporal scales. (A) Within-year dynamics linking phenology, canopy development (NDVI = black; LAI = green), environmental forcing, and reproductive timing; the yellow bar indicates the temperature cue sensing window, the grey bell-shaped curve flowering and pollination, and the purple curve seed development; (B) Conceptual representation of reproductive allocation and environmental filtering, where carbon allocated to flowers and seeds may be reduced by pollination failure or drought, with unused resources retained in the internal budget; (C) Multi-year schematic showing how temperature cues from the two preceding years (Y-1 and Y-2; orange bars) contribute to reproductive potential in

year Y. Grey lines show flowering, the purple line seed development, and the black line NDVI.

Precipitation during the flowering window may reduce pollination efficiency (Sofiev *et al.*, 2013), while drought during seed development can limit seed filling, acting as an environmental veto on carbon conversion (Figure 2B; Bogdziewicz *et al.*, 2018). Carbon not successfully converted into seeds is retained in the internal budget, linking successive years through resource carry-over that interacts with prior reproductive costs and lagged climatic forcing (Figure 2C).

Environmental regulation is introduced through temperature cues derived from the interannual contrast in post-solstice maximum air temperatures, based on the evidence that warmer summers in the year immediately preceding seed production are the climatic signal most reliably associated with mast seeding in European beech (Kelly *et al.*, 2013; Vacchiano *et al.*, 2017; Journé *et al.*, 2024; Hirsch *et al.*, 2025). For each simulation year, the mean daily maximum air temperature is computed over a fixed post-solstice window spanning days of year 172–212 (21 June – 31 July). The inter-annual temperature anomaly is defined as $\Delta T = T_{Y-1} - T_{Y-2}$, where T_{Y-1} is the mean post-solstice temperature of the year immediately preceding seed production and T_{Y-2} is the corresponding value two years prior. The weather cue (WC) is computed from ΔT via a Gompertz function (Equation 2)

$$WC_t = A \times \exp\{-\exp[-k \times (\Delta T - \mu)]\} \quad [2]$$

where $k = 2$ is a fixed sensitivity parameter governing the steepness of the response, estimated empirically by maximising the Pearson correlation between ΔT and observed interannual variability in seed production across the 11 study sites, and fixed prior to calibration of the reproductive component parameters; $\mu = (\Delta T_{min} + \Delta T_{max}) / 2$ is the midpoint of the site-specific range of interannual temperature anomalies (with ΔT_{min} and ΔT_{max} set to the minimum and maximum ΔT observed across the historical weather record), and A is the asymptote. WC_t increases monotonically with ΔT: positive post-solstice summer ΔT promotes reproductive investment, negative post-solstice summer ΔT suppresses it (Supplementary Material S2).

Three model variants differing in their reproductive allocation scheme have been implemented and tested. In the baseline formulation (RB), no weather cue is used and reproductive investment is governed exclusively by BL_t; i.e., governed by resource dynamics only. The two weather-cue variants extend this baseline by incorporating weather cues (WC_t) (Equation 2), but differ in the choice of asymptote A. In the RB+WC formulation, $A = 1$, so $WC_t \in [0, 1]$ independently of the resource state: a sufficiently strong temperature signal can saturate the weather cue regardless of carbon reserves. In the RB×WC formulation, $A = BL_t$, so WC_t is bounded by the current budget level and a favourable temperature signal can only promote reproduction in proportion to accumulated reserves, producing a resource-gated response. In both weather-cue variants WC_t is clipped to [0, 1].

Annual reproductive investment (I_{rep}, g C m^{-2}) is determined at the end of each year and constrained by both reproductive potential and available carbon (Equation 3):

$$I_{rep} = \min\left(B_t,\ B_{max} \cdot \frac{(1-CUE_w)\times BL_t + CUE_w \times WC_t}{2}\right) \quad [3]$$

where CUE_w is a weighting coefficient balancing the contribution of the resource budget and the weather cue (set to 0 in the RB variant). I_{rep} is partitioned into a flowering investment (I_{fl}) and a seed maturation investment (I_{mat}) as $I_{mat} = I_{rep} / (1 + FFC)$ and $I_{fl} = I_{rep} - I_{mat}$, where FFC is a calibrated cost ratio of flowers to fruit. While carbon is not the only resource potentially limiting reproduction, the budget used here functions as an integrative proxy for physiological readiness; explicit representation of nutrient cycles is beyond the current scope (Kabeya, 2021; Végh & Kato, 2024).

Pollination dynamics are simulated daily within the flowering window, defined as the interval centred on FLO_t with half-width $FLO_d / 2$, expressed as a percentage of the growth phase, where FLO_t and FLO_d are the timing and duration of peak pollen release. Daily pollination potential follows a Gaussian curve centred on FLO_t, and actual pollination is modulated by a logistic function of daily precipitation that decreases below a calibrated limiting threshold (POL_p, mm). At flowering completion, both I_{fl} and I_{mat} are scaled by the cumulative pollination efficiency, so that poor pollen transfer directly reduces the carbon committed to seeds while retaining the remainder in the budget. Seed maturation proceeds subsequently during the leaf senescence phase through a sigmoidal function of the canopy greendown percentage, modulated daily by a water stress coefficient, converting I_{mat} into the final seed carbon output. Unrealised seed carbon (due to drought stress during maturation) is retained in the resource budget and carried forward to the following year.

2.2. Calibration and evaluation

2.2.1. Input data

Model calibration and evaluation were performed using 2,925 individual-tree-level observations from 97 European beech trees collected across 11 locations in the UK (Hacket-Pain *et al.*, 2025; Supplementary Material S3). Sites span a latitudinal gradient from Woodbury in the southwest to Benwell in the northeast, covering a range of climatic conditions representative of the UK beech distribution. Each site included between 5 and 12 monitored trees (after excluding individuals with fewer than 10 years of observations), with observation periods ranging from 1980 to 2025 (Supplementary Material S3). Seed production and DBH were measured during field sampling and from tree-ring records, as detailed in Packham *et al.* (2008), Bogdziewicz *et al.* (2023) and Hacket-Pain *et al.* (2025). Seed production data from 1980–2022 were used for model calibration and hypothesis testing, while data from 2023–2026 were reserved for prospective forecasting evaluation.

To parameterise the phenological model, vegetation dynamics were derived from remotely sensed MODIS NDVI imagery at 250 m resolution (8-day maximum value composite; Holben, 1986) over the period 2001–2022, processed using the MODISTools R package (Hufkens, 2023). Daily air temperature (°C) and precipitation (mm) were obtained for each site from the ERA5 reanalysis dataset (Copernicus Climate Change Service), accessed via Google Earth Engine (Gorelick *et al.* 2017). Incoming solar radiation (MJ m^{-2} d^{-1}) was estimated from daily temperature range using the Hargreaves–Samani equation (Hargreaves & Samani, 1985), with extraterrestrial radiation calculated from site latitude and day of year, ensuring applicability in the absence of measured or reanalysis-derived radiation data and extending the model transferability to contexts where only temperature and precipitation observations are available.

2.2.2. Simulation experiments

A global sensitivity analysis using the Morris One-At-a-Time method (Morris, 1991) was performed prior to calibration to identify the parameters exerting the greatest influence on model outputs and to fix non-influential ones at reference values. The analysis was conducted separately for each of the 11 sites, using two target variables characterising fundamental features of reproductive dynamics: mean long-term carbon allocated to seeds (C_{seed}), and the coefficient of variation of interannual seed production (CV_{seed}). Parameters spanned all model modules, including photothermal thresholds governing phenological phases given their linkage to resource accumulation (Table 1).

Variation ranges were derived from published literature values where species-specific estimates were available; for parameters specific to MASTHING, ranges were defined as biologically plausible intervals refined through a preliminary screening calibration run. For each parameter, two summary statistics were computed: the mean absolute elementary effect (μ*, Campolongo *et al.*, 2007), quantifying average influence on the target variable, and the standard deviation of elementary effects (σ), reflecting non-linearity and parameter interactions. The analysis used r = 100 trajectories with a 6-level design (grid jump = 3), implemented via the *morris()* function in the *sensitivity* R package (Iooss *et al.*, 2026).

The seven parameters selected for calibration of the reproductive component were ECO, LUE, RBF, FLO_t, FLO_d, POL_p, and REP_{thr} (Table 1). The photothermal thresholds governing NDVI-defined phenological phases (GRO, GRD, SEN) did not emerge as influential and were fixed following a prior calibration against MODIS NDVI time series (Section 2.2.3). The diameter at breast height (DBH) was included as an observed tree-level covariate and assigned its measured value for each study tree. Its influence on carbon dynamics is implicitly captured through the resource budget

fraction (RBF), which was calibrated to account for systematic variation in surplus carbon directed to reproduction as a function of tree size.

Table 1. Parameters included in the global sensitivity analysis. SA range: variation interval used during the sensitivity analysis. For parameters with established empirical bases, ranges were derived from literature values (sources in footnotes); for parameters specific to MASTHING, ranges were fixed as biologically plausible intervals and refined through a preliminary screening calibration run (denoted F); 'Observed' = set to the 10^{th} – 90^{th} percentile range of measured tree DBH across sites.

Module	Symbol	Description	SA range	Source
Phenology	ECO	Ecodormancy photothermal threshold (days)	4 – 10	1
	GRO	Growth photothermal threshold (days)	40 – 50	1
	GRD	Greendown photothermal threshold (days)	85 – 95	1
	SEN	Senescence photothermal threshold (days)	55 – 65	1
Resources	LUE	Light use efficiency (g DM MJ^{-1})	1.2 – 2	2, 3
	T_{heat}	Critical heat temperature (°C)	35 – 40	4
	T_{cold}	Critical cold temperature (°C)	0 – - 2	5
	RBF	Resource budget fraction (–)	0.30 – 0.45	F
	WS_{thr}	Water stress threshold (–)	0.50 – 0.60	F
	RES_w	Relative wood respiration (day^{-1})	0.0001 – 0.0003	6
	RES_l	Relative leaf respiration (day^{-1})	0.02 – 0.04	7
	Q_{10}	Temperature sensitivity of respiration (–)	1.5 – 2.5	8
	SLA	Specific leaf area ($m^2\ kg^{-1}$)	16.5 – 26.5	9
	ALL_w	Wood allocation fraction maximum (–)	0.40 – 0.50	F
	RNG_w	Ring width conversion factor (mm $g^{-1}\ m^{-2}$)	0.001 – 0.004	F
Reproduction	FLO_t	Flowering onset time (% growth phase)	0 – 10	10
	FLO_d	Flowering duration (% growth phase)	5 – 15	11
	POL_p	Pollination precipitation limit (mm)	5 – 15	F
	FFC	Flower-to-fruit cost (–)	0.18 – 0.29	12
	CUE_s	Temperature cue sensitivity (–)	1.5 – 2.5	F
	CUE_w	Temperature cue weight (–)	0.45 – 0.55	F
	REP_{thr}	Reproduction threshold (–)	0.50 – 0.70	F
Allometry	DBH	Diameter at breast height (cm)	56 – 120.3	O

1: Bajocco et al. (2025); 2: Yuan et al. (2007); 3: Fibbi et al. (2019); 4: Hauck et al. (2025); 5: Vitasse et al. (2025); 6: Running and Hunt (1993); 7: Penning de Vries et al. (1989); 8: Damesin (2003); 9: Forrester et al., 2017; 10: Gömöry and Paule (2011); 11: Bogdziewicz et al. (2017); 12: Isagi et al. (1997)

Three model formulations were compared: a resource-budget-only model (RB), and two extensions incorporating weather cues with additive (RB+WC) and interactive (RB×WC) effects on reproductive allocation (Section 2.1.1). These represent alternative ecological hypotheses regarding the mechanism underlying mast seeding; in particular, RB×WC assumes that sensitivity to weather

cues depends on internal resource status. Comparing model performance across formulations therefore constitutes a test of these hypotheses rather than a conventional model selection exercise.

For each formulation, three parameterisation strategies were applied: Tree-level, where parameters were calibrated independently per tree, capturing phenotypic variation but not transferable to unsampled individuals; Site-level, where a single parameter set was defined for each site, assuming shared physiological response to local climate; and Country-level, where a single parameter set was calibrated across all 11 sites, assuming species-wide transferability. This yielded nine model configurations in total (three formulations × three strategies). All simulations were performed at the individual tree level, and outputs were aggregated to the site-year level as the mean normalised reproductive investment across trees within each site and year.

2.2.3. Calibration methodology

Calibration was performed in two sequential steps. In the first step, the photothermal thresholds governing growth, greendown, and senescence phases (GRO, GRD, SEN) and NDVI modulators were optimised against MODIS NDVI time series following the procedure described in Bajocco et al. (2025), using all available NDVI observations to maximise signal for phenological estimation. The resulting site-level phenological parameters were then held fixed throughout all subsequent model runs.

In the second step, the seven reproductive component parameters identified by the sensitivity analysis (Section 2.2.2) were optimised against seed production data using a multi-start Nelder-Mead simplex algorithm with 50 independent runs per configuration. All available observations from 1980–2022 were used for calibration to maximise the ecological signal, with prospective forecasting performance evaluated independently on the 2023–2026 data (excluded from all calibration stages). To minimise sensitivity to initial resource budget conditions, each simulation was preceded by a ten-year spin-up period in which climate forcing from 1978 was repeated cyclically, allowing the carbon budget and allometric state variables to reach a quasi-equilibrium before the calibration window began. The calibration objective function combined four metrics: RMSE of normalised seed production (weight 0.30), one minus the Pearson correlation between simulated and observed seed production (weight 0.50), one minus the Pearson correlation between simulated and observed DBH (weight 0.10), and RMSE of DBH (weight 0.10). Calibration was performed independently under each of the three parameterisation strategies described in Section 2.2.2.

2.2.4. Model evaluation framework

Model performance was assessed at multiple levels, with all metrics calculated at the site-year level as the mean normalised reproductive investment across trees within each site and year. Inter-annual variability in seed production was first evaluated through the proportion of variance explained (R^2) between simulated and observed normalised seed production, computed both per site and pooled across all sites and stratified by calibration level; R^2 quantifies the fraction of observed interannual variance that the model reproduces, ranging from 0 (no explanatory power) to 1 (perfect agreement).

The capacity of each formulation to correctly classify years into discrete reproductive categories was then assessed by assigning normalised site-mean seed production to one of four classes: Failure [0, 0.25), Low [0.25, 0.50), High [0.50, 0.75), and Mast [0.75, 1], whose boundaries correspond to quartiles of the normalised scale. Agreement between simulated and observed class assignments was quantified using Overall Accuracy (OA = (TP + TN) / N), quadratic-weighted Cohen's κ (κ^w), which penalises large misclassifications more strongly than adjacent-class errors, and Matthews correlation coefficient (MCC = (TP × TN – FP × FN) / √((TP+FP)(TP+FN)(TN+FP)(TN+FN))), which provides a balanced measure robust to class imbalance. In these expressions, TP (true positives), TN (true negatives), FP (false positives), and FN (false negatives) are computed for each class treated as the positive outcome, and N is the total number of observations. Class-specific performance was further characterised by probability of detection (POD = TP / (TP + FN)), specificity (TN / (TN + FP)), precision (TP / (TP + FP)), F1 score (2TP / (2TP + FP + FN)), and critical success index (CSI = TP / (TP + FP + FN)).

Temporal dynamics of simulated seed production were evaluated against annual observed medians using the Nash–Sutcliffe model efficiency ($ME = 1 - \Sigma(O - S)^2 / \Sigma(O - \bar{O})^2$, where O is observed, S is simulated, and $\bar{O}$ is the observed mean), which expresses predictive skill relative to the climatological mean as a baseline: ME = 1 indicates perfect simulation, ME = 0 means the model performs no better than the observed mean, and negative values indicate worse performance than the mean. Temporal agreement was additionally characterised by the Pearson correlation coefficient (r), root mean square error ($RMSE = \mathrm{sqrt}(\mathrm{mean}(S - O)^2)$), and systematic bias ($Bias = \mathrm{mean}(S - O)$).

The ability of MASTHING to reproduce long-term changes in masting intensity under climate warming was evaluated through a moving-window analysis. The population-level coefficient of variation (CV_p) of mean normalised annual seed production across trees was averaged across sites over 10-year windows with a 5-year step, and the proportion of failure years (site-mean normalised seed production below 0.25) was computed over the same windows. These statistics capture, respectively, the amplitude of interannual synchrony in seed production and the frequency of near-

zero crop years. Agreement between simulated and observed window-level statistics was quantified with R^2.

The structural realism of the model was further assessed by evaluating its ability to reproduce two variables not used as primary calibration targets: simulated NDVI seasonal dynamics were compared with MODIS observations using RMSE and Pearson correlation, and simulated DBH trajectories were compared with dendrochronological records across DBH size classes. These comparisons provide an independent check on the phenological and allometric components of the model, ensuring that the resource budget underpinning reproductive allocation is driven by realistic phenology and carbon assimilation dynamics.

3. Results

3.1. Sensitivity analysis and parameter selection for calibration

Sensitivity indices μ* and σ computed per site and model formulation, and their cross-site means, are reported for the eight most relevant parameters modulating mean carbon allocated to seeds (C_{seed}) and coefficient of variation (CV_{seed}) in Figure 3. Full sensitivity results are provided in Supplementary Material S4.

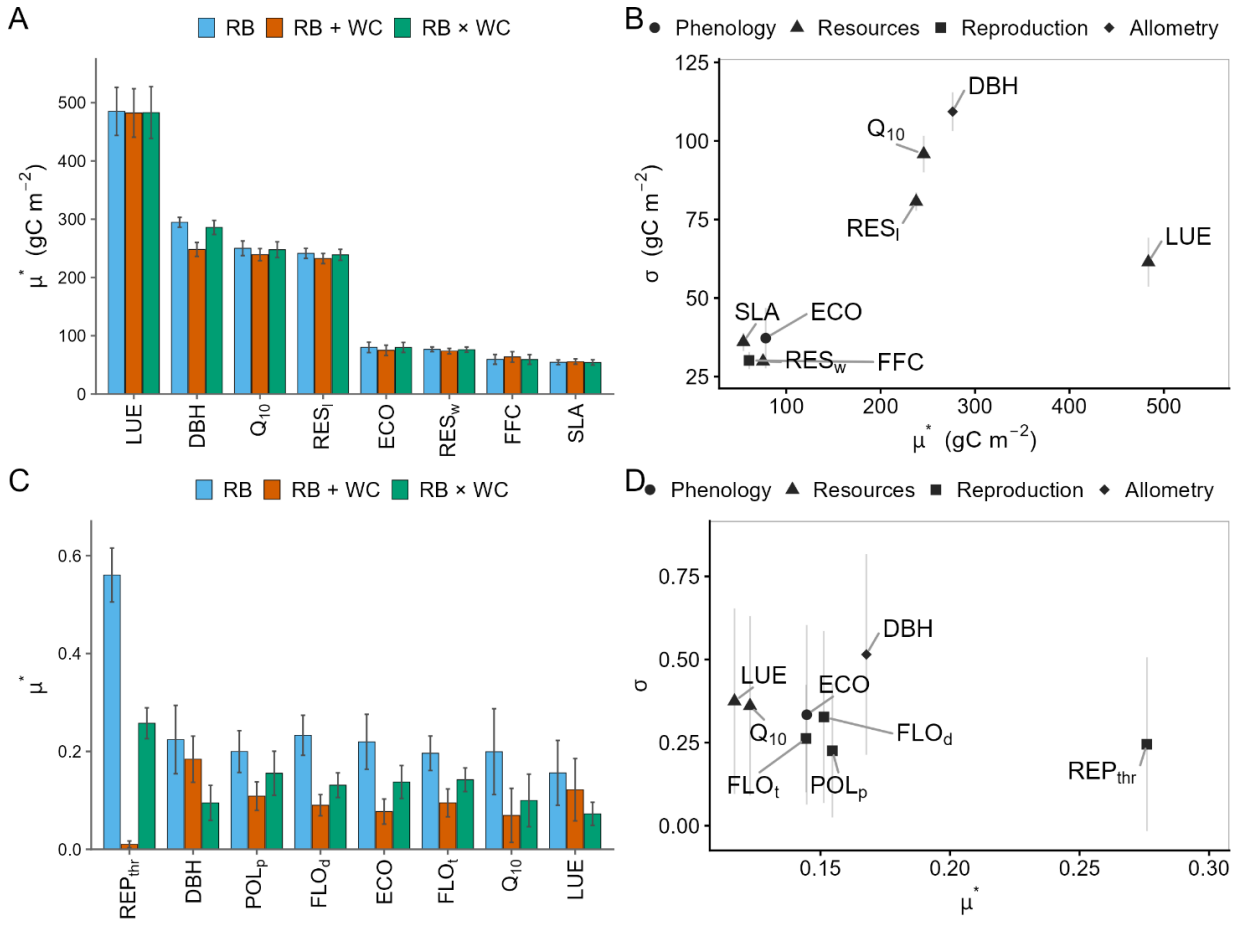

Figure 3. Results of the Morris global sensitivity analysis for the two main target variables: mean annual seed production (panels A–B) and its interannual coefficient of variation (panels C–D). The eight parameters with the highest mean absolute elementary effect (μ*), averaged across sites and formulations, are shown for each variable. Acronyms for each parameter are explained in Table 1. Panels A, C: mean μ* per formulation (bars) for the top-ranked parameters, ordered by decreasing μ*; bar height represents the mean across the 11 study sites and error bars standard deviation. Panels B, D: μ*–σ scatter plots summarising both the magnitude (μ*, x-axis) and the degree of non-linearity and parameter interactions (σ, y-axis) for the same eight parameters; each point represents the global mean across sites and formulations, and vertical error bars show the corresponding standard deviations.

For C_{seed}, light use efficiency (LUE; μ* = 484 g C m^{-2}) was the most influential parameter by a large margin, with a relatively low σ (61 g C m^{-2}) consistent with predominantly linear and additive effects on carbon assimilation (Figure 3A-B). Three parameters formed a secondary cluster: tree diameter at breast height (DBH; μ* = 276 g C m^{-2}), the temperature sensitivity coefficient of respiration (Q_{10}; μ* = 246 g C m^{-2}), and relative leaf respiration rate (RES_l; μ* = 238 g C m^{-2}), all with markedly higher σ (80–109 g C m^{-2}), indicating non-linear responses and interactions among carbon-balance parameters. A third tier comprising ecodormancy photothermal threshold (ECO; μ* = 78 g C m^{-2}), relative wood respiration (RES_w; μ* = 75 g C m^{-2}), flower-to-fruit conversion cost (FFC; μ* = 61 gC m^{-2}), and specific leaf area (SLA; μ* = 55 g C m^{-2}) contributed at an intermediate but non-negligible level. Sensitivity rankings for C_{seed} were consistent across model formulations, and all remaining parameters had μ* < 50 g C m^{-2} and were considered non-influential (Supplementary Material S4).

For CV_{seed}, the reproduction threshold (REP_{thr}; mean μ* = 0.28 across formulations) was the most relevant parameter, but its absolute sensitivity differed markedly across formulations, reflecting how each variant couples the resource budget to the weather cue (Figure 3C-D). REP_{thr} influences CV_{seed} through two complementary mechanisms (Equation 1). First, it sets a binary threshold: below $B_{min} = REP_{thr} \times B_{max}$, $BL_t = 0$ and no reproductive investment occurs, directly controlling the frequency of zero-seed years. Second, a higher REP_{thr} raises B_{min}, reducing the range ($B_{max} - B_{min}$, the denominator in Equation 1) over which BL_t varies and making the same interannual carbon fluctuation translate into a larger difference in reproductive investment, therefore sharpening the contrast between years of moderate and high resource accumulation. These two mechanisms increase year-to-year variability in seed production without changing its long-term mean, explaining why REP_{thr} dominates CV_{seed} while remaining nearly irrelevant for C_{seed} (μ* ≈ 10 g C m^{-2}).

How these mechanisms propagate depends on the model formulation. In the baseline RB variant, both effects act directly and exclusively through BL_t, yielding the highest sensitivity (μ* ≈ 0.57). In RB×WC, the weather cue asymptote $A = BL_t$ (Equation 2) means that $WC_t = 0$ whenever $BL_t = 0$, so

411 the threshold effect is preserved as a necessary condition for any reproductive allocation, and the
412 slope effect also carries through the weather cue term; sensitivity remains high ($\mu^* \approx 0.27$) but is
413 reduced because the Gompertz response introduces variability that partially decouples from the
414 carbon scale. In RB+WC, REP_{thr} becomes far less influential ($\mu^* \approx 0.13$) because the cue asymptote
415 is fixed at A = 1: WC_t remains positive even when $BL_t = 0$, so reproductive investment can occur
416 regardless of whether the carbon threshold is crossed, bypassing the threshold effect; since the
417 weather cue term (weighted by CUE_w) in Equation 3 operates independently of BL_t, the slope effect
418 of REP_{thr} propagates through only the $(1 - CUE_w)$ fraction of total reproductive potential.
419 DBH exhibited the highest absolute σ for CV_{seed} ($\sigma = 0.52$), far exceeding its μ^* (0.17), indicating
420 strongly non-linear, site-contingent effects on interannual seed variability. Pollination precipitation
421 limit (POL_p; $\mu^* = 0.16$), flowering duration (FLO_d; $\mu^* = 0.15$), ecodormancy threshold (ECO; $\mu^* =$
422 0.15), and flowering onset time (FLO_t; $\mu^* = 0.14$) showed broadly comparable influence, all with
423 elevated σ (0.23–0.37) reflecting non-linear dynamics and interactions.
424 The recurrent appearance of LUE, DBH, Q10, and ECO among the top-ranked parameters for
425 both target variables identifies carbon-balance, allometric, and phenological processes as the
426 dominant sources of variability in both the mean level and the temporal dynamics of seed production,
427 albeit through contrasting mechanisms. LUE dominated C_{seed} ($\mu^* = 484$ g C m^{-2}) with a
428 predominantly linear influence on carbon assimilation (low σ) yet expressed its effect on CV_{seed}
429 primarily through non-linear interactions ($\sigma \approx 0.55$). DBH ranked second for both variables, with high
430 σ in both cases, reflecting its role in setting individual tree size and thus the absolute carbon
431 assimilation capacity. ECO showed comparable influence across both variables through its control
432 over the onset of the growing season, affecting both mean productivity and year-to-year variability.
433 By contrast, REP_{thr} was negligible for C_{seed} ($\mu^* \approx 10$ g C m^{-2}) but the leading driver of CV_{seed}, and
434 POL_p, FLO_d, and FLO_t appeared exclusively among the top-ranked parameters for CV_{seed}, indicating
435 that pollination-window timing and duration are mechanisms specifically relevant to interannual
436 variability rather than to mean productivity. Temperature-related parameters (T_{heat}, T_{cold}) had
437 consistently low μ^* across both variables, suggesting that thermal stress thresholds have limited
438 global influence under the parameter ranges and environmental conditions tested.
439 These results directly informed the selection of parameters for model calibration. Seven
440 parameters were retained based on their sensitivity and mechanistic relevance to beech reproductive
441 ecology: ECO, LUE, REP_{thr}, FLO_t, FLO_d, and POL_p, and the resource budget fraction (RBF).
442 Although DBH ranked second for both target variables, it enters the model as a measured input rather
443 than a free parameter; RBF was therefore included as its functional surrogate, since it scales
444 maximum resource storage capacity directly to individual tree biomass and thus captures the

allometric control over reproductive potential that DBH reflects in the sensitivity analysis. All remaining parameters were held at literature-derived or allometrically constrained values (Supplementary Material S4).

3.2. Comparative performance of model formulations across calibration strategies

The proportion of variance in carbon allocated to seed production explained by the three formulations differed markedly depending on both the model structure and the calibration strategy (Figure 4). The interactive formulation (RB×WC) achieved the highest R^2 across all three calibration levels (country, site, and tree; Figure 4A-C).

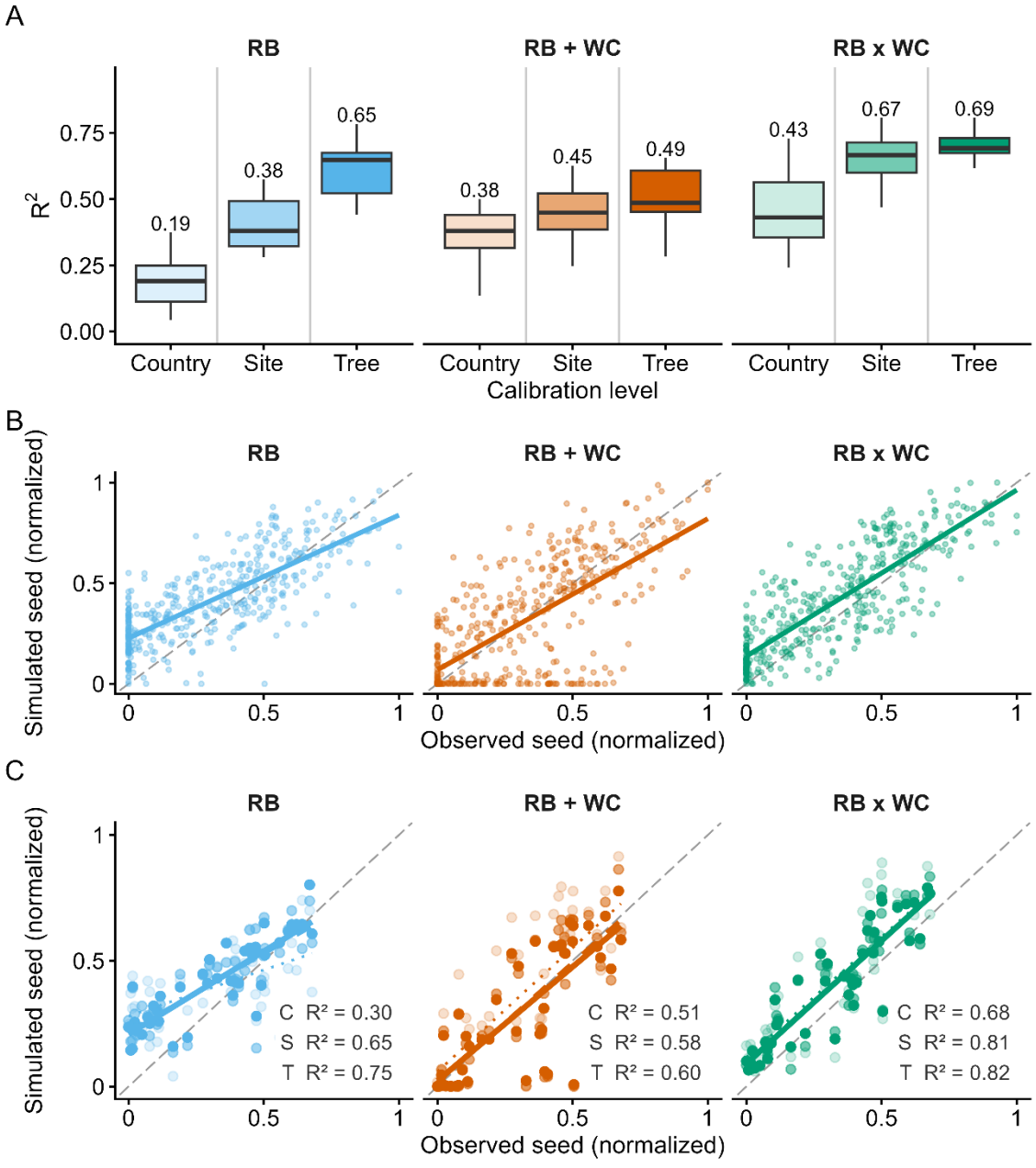

Figure 4. Correlation between observed and simulated normalised seed production across model formulations and calibration strategies. (A) Distribution of per-site R^2 for the resource-budget-only model (RB; blue), the additive weather-cue model (RB+WC; orange), and the interactive weather-cue model (RB×WC; green), stratified by calibration level (Country, Site, Tree). Numbers above whiskers indicate the median per-site R^2. (B) Observed vs. simulated normalised seed production at the site-year level under tree-level calibration; points are semi-transparent to show density, lines show fitted linear regressions. (C) Same relationship aggregated to the annual level; regression lines are shown separately for each calibration strategy (C = Country, S = Site, T = Tree), with R^2 values reported in the inset. The dashed 1:1 line indicates perfect agreement in all scatter panels.

The additive formulation (RB+WC) improved over the resource-budget-only baseline (RB) only under country-level calibration (R^2 = 0.34 vs. 0.12, Figure 4A; R^2 = 0.51 vs. 0.30, Figure 4C). At site- and tree-level calibration its explained variance was comparable to or lower than RB (site level: R^2 = 0.41 vs. 0.40; tree level: R^2 = 0.45 vs. 0.59, Figure 4A), indicating that incorporating a weather cue whose effect is independent of the resource state does not improve, and can even reduce, predictive skill when the model is calibrated at fine spatial scales, where the resource budget alone already captures much of the observed inter-annual variability. This pattern suggests that weather acts as a dominant, "overriding" signal at coarse spatial scales, where it compensates for individual variability not yet captured by RB, but becomes misaligned once that individual variability is already well represented, as is the case at finer calibration levels. The RB×WC model avoided this degradation by scaling the cue amplitude to the current resource state, so that a favourable temperature anomaly enhances reproduction only when carbon reserves are sufficient to support it. By letting weather modulate rather than simply add to the individual response, this formulation avoided the conflict seen in the additive model and instead improved consistently across calibration levels, with the largest relative gains observed precisely at the finer scales (Figure 4A). Accordingly, the reduction in explained variance from tree- to country-level calibration was modest for RB×WC (R^2 = 0.82 to 0.68 at the annual scale, Figure 4C), indicating that the processes captured by this formulation are largely transferable across the observational network rather than site-specific.

Site-level performance across all formulations and calibration strategies are detailed in Supplementary Material S5, whereas calibrated parameter values across sites, calibration levels, and model versions are reported in Supplementary Material S6.

The ranking among model formulations was confirmed by classification-based metrics (Table 2; Figure 5).

Table 2. Per-class classification performance of the three model versions across calibration levels. Each row corresponds to one seed production class within one model–calibration combination. POD: Probability of Detection; CSI: Critical Success Index. Bold font indicates the best performance for each metric at each calibration level.

Calibration	Model	OA	κ	MCC	POD	Specificity	Precision	F1	CSI
Country	RB	0.349	0.253	0.121	0.324	0.784	0.347	0.308	0.186
	RB + WC	**0.445**	0.430	0.197	**0.384**	0.807	0.364	0.366	0.239
	RB × WC	0.435	**0.479**	**0.210**	**0.384**	**0.813**	**0.386**	**0.376**	**0.244**
Site	RB	0.374	0.434	0.165	0.371	0.797	0.406	0.360	0.223
	RB + WC	**0.496**	0.499	0.241	0.402	0.818	0.394	0.397	0.266
	RB × WC	0.494	**0.604**	**0.303**	**0.467**	**0.836**	**0.470**	**0.454**	**0.305**
Tree	RB	0.454	0.566	0.261	0.454	0.822	0.460	0.437	0.287
	RB + WC	**0.530**	0.582	0.292	0.458	0.828	0.457	0.458	0.312
	RB × WC	**0.530**	**0.674**	**0.336**	**0.489**	**0.845**	**0.483**	**0.479**	**0.331**

Performance improved monotonically with calibration granularity (Country < Site < Tree) across all model versions and metrics, with the largest relative gains observed in chance-corrected measures (κ, MCC) rather than OA. This scale effect was most pronounced for RB×WC, whose advantage over the additive model (RB+WC) grew larger at finer calibration levels, suggesting that reproductive biology-weather interactions become increasingly detectable as spatial resolution increases from country-wide averages to tree-specific data.

Under tree-level calibration, RB×WC obtained a quadratic-weighted κ of 0.674 and MCC of 0.336, compared to κ = 0.582 and MCC = 0.292 for RB+WC, and κ = 0.566 and MCC = 0.261 for RB. Despite broadly similar overall accuracy (OA ≈ 0.53 for both weather-cue models; 0.454 for RB), κ and MCC, which account for chance agreement and class imbalance respectively, revealed a consistent advantage for the interactive formulation at all calibration levels (Table 2).

Per-class analysis revealed that RB+WC substantially increased failure year detection (POD: 71% vs. 47% for RB) but at the cost of reduced accuracy for intermediate and high-seed classes (Figure 5A, Supplementary Material S6). RB×WC achieved a more balanced improvement: failure detection reached 64% while mast year detection improved to 54% (vs. 51% for RB and 48% for RB+WC), indicating that the resource-modulated cue enhances discrimination at both extremes of the seed production range without degrading intermediate categories. Classification skill decreased progressively from tree- to country-level calibration across all formulations, with RB×WC retaining the largest advantage in κ at site level (0.60 vs. 0.50 for RB+WC and 0.43 for RB), while at country level all formulations showed reduced skill (κ between 0.25 and 0.48) (Supplementary Material S7).

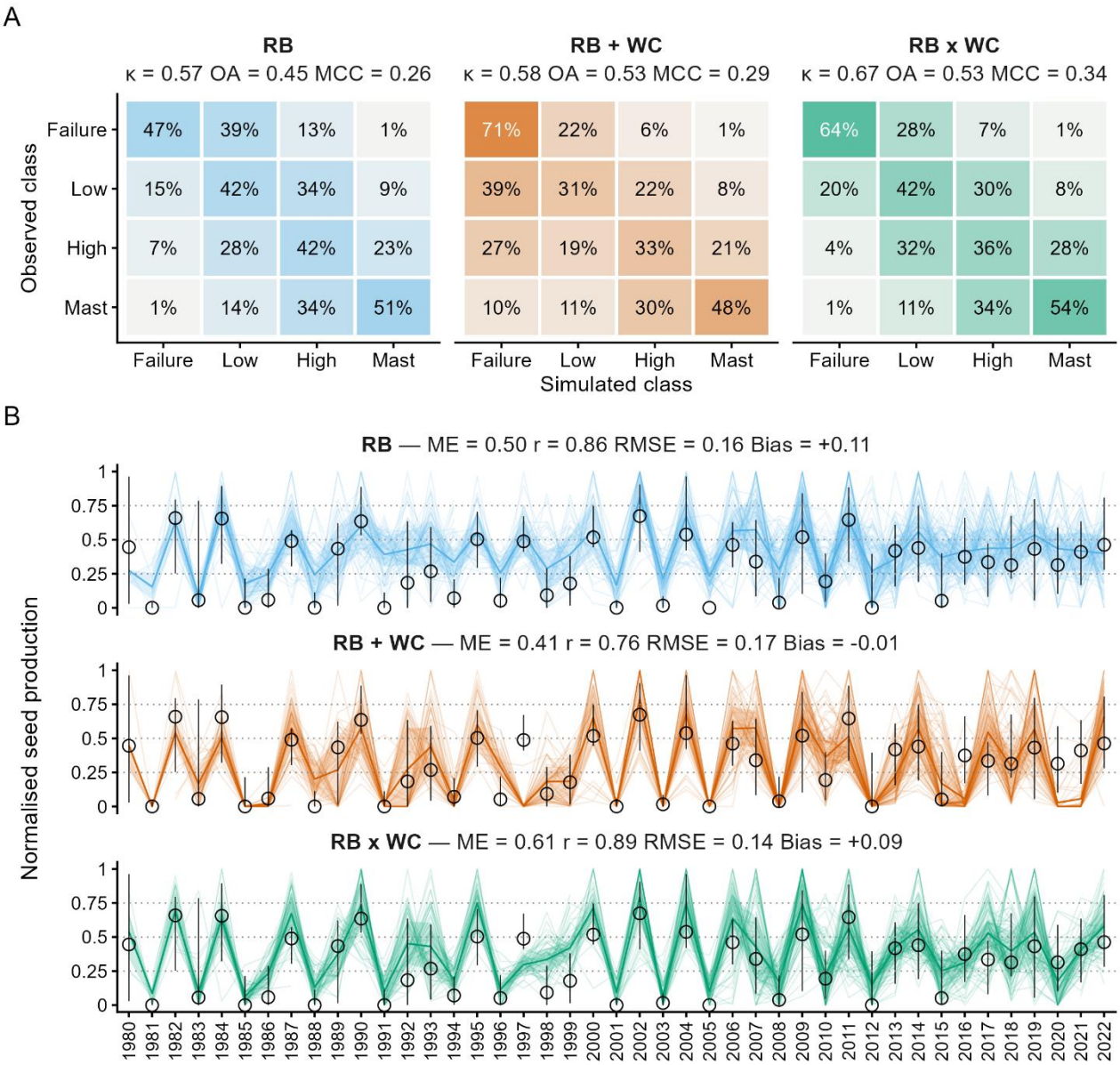

Figure 5. Classification performance and temporal dynamics of the three model formulations under tree-level calibration. (A) Confusion matrices showing the distribution of simulated seed production classes conditional on observed class (row percentages). Seed production is classified into four classes based on normalised values: Failure [0–0.25), Low [0.25–0.5), High [0.5–0.75), and Mast [0.75–1]. Colour intensity within each model panel scales with row percentage (white = 0%, full model colour = 100%). Overall performance metrics shown above each panel: quadratic-weighted Cohen's κ, Overall Accuracy (OA), and Matthews Correlation Coefficient (MCC). (B) Annual time series of normalised seed production under tree-level calibration. Thin coloured lines show individual tree trajectories; darker and lighter shaded bands indicate the 40–60th and 25–75th percentile intervals of simulated values respectively. Black points and bars show the observed median and interquartile range across site-year means. Horizontal dotted lines mark class boundaries at 0.25, 0.5, and 0.75. Strip labels report model efficiency (ME), Pearson correlation (r), RMSE, and bias computed between annual medians of simulated and observed values.

The temporal dynamics of simulated seed production (Figure 5B) confirmed these patterns. RB×WC achieved the highest model efficiency (ME = 0.61) and Pearson correlation with annual observed medians (r = 0.89, RMSE = 0.14), with a modest positive bias (Bias = +0.09) reflecting a

slight overestimation of median production. RB showed comparably high temporal correlation (r = 0.86) but lower model efficiency (ME = 0.50) and a larger positive bias (Bias = +0.11), consistent with its tendency to compress the dynamic range of simulated seed production. RB+WC had the lowest temporal correlation (r = 0.76) and model efficiency (ME = 0.41), despite negligible bias (Bias = −0.01), suggesting that unconstrained weather cues disrupt the inter-annual timing of reproductive cycles.

The internal consistency of auxiliary model outputs was assessed independently of seed production. Simulated seasonal NDVI dynamics closely reproduced satellite-derived observations across sites (r = 0.98, RMSE = 0.021), and the interannual NDVI time series (2003–2023) showed strong agreement with observed values (r = 0.94, RMSE = 0.039), confirming that the phenological and carbon-balance modules produce realistic canopy development trajectories (Supplementary Material S8). Simulated DBH trajectories preserved the rank order of size classes across the full ~40-year simulation period and captured the expected positive growth trends within each class, providing independent support for the carbon partitioning scheme and for the multi-year trade-off between reproductive investment and radial growth.

3.3. Resource budget and weather cue interactions in simulated seed carbon allocation

The three formulations generated qualitatively distinct relationships between weather cue intensity and normalised seed production (Figure 6A). In RB, the fitted exponential ($y = 0.26 \times 1.41^{WC}$) had the highest intercept among the three formulations and the lowest base, indicating that seed allocation was sustained even at near-zero cue values and increased only modestly with cue intensity. The base of 1.41 implies a 41% increase in predicted allocation from WC = 0 to WC = 1, the weakest cue sensitivity of all formulations. This is consistent with the absence of an explicit cue mechanism in RB: seed output is governed almost entirely by resource availability, and the apparent relationship with the cue signal is a residual effect of the cue co-varying with growing-season conditions. The heatmap confirms this interpretation: the allocation surface is structured predominantly along the budget axis, with the highest normalised values concentrated in the upper region regardless of cue conditions, and no coherent gradient along the cue axis (Figure 6B).

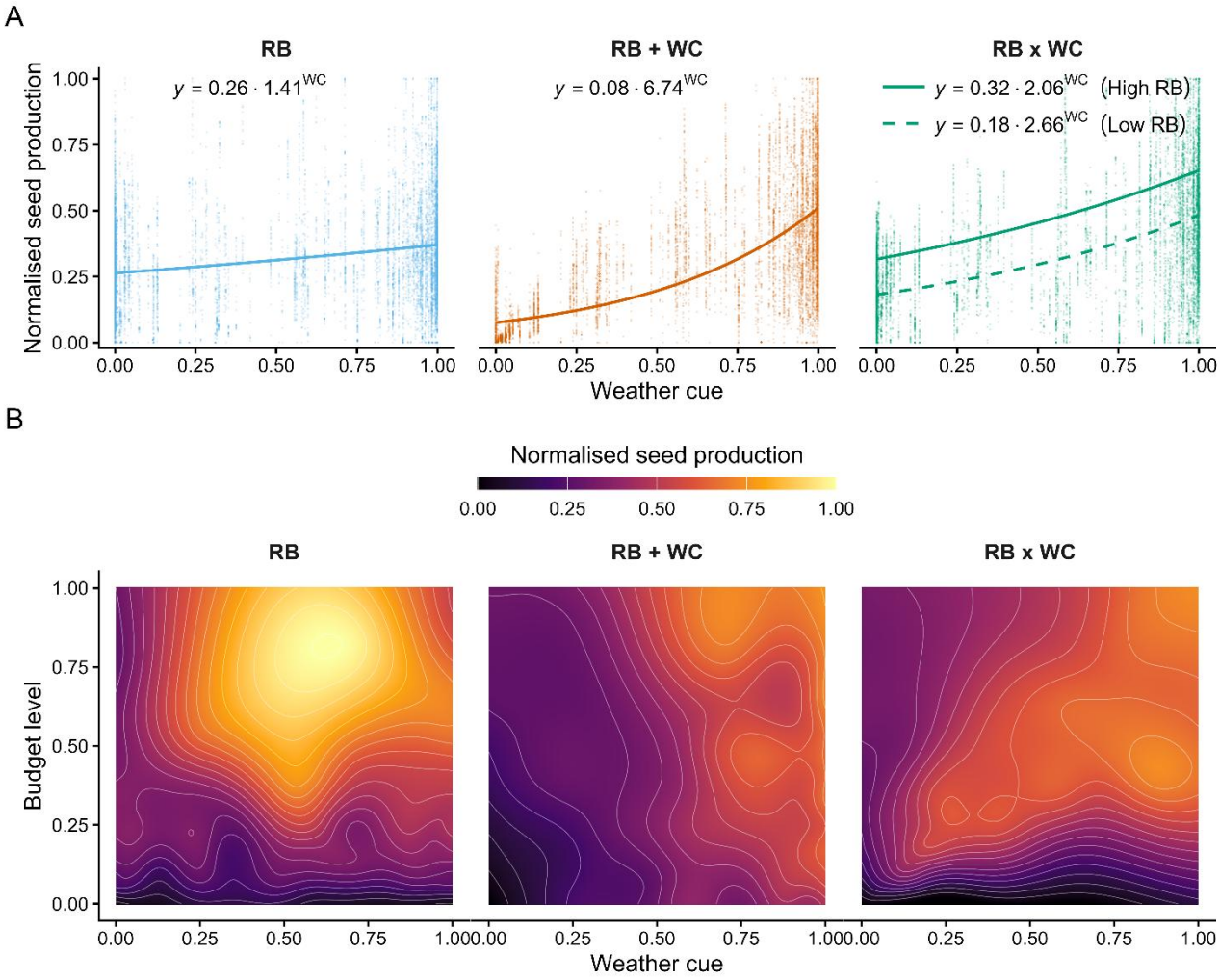

Figure 6. Joint effects of resource budget level and weather cue intensity on normalised simulated seed production. (A) Relationship between weather cue intensity and site-normalised seed production (min–max scaled per pixel and model formulation, where 0 = minimum and 1 = maximum annual production) across model formulations. Points represent individual tree-year simulations; lines show fitted exponential functions ($y = a \times b^{WC}$). In the RB×WC formulation, separate curves are shown for trees with high (solid line, budget level ≥ 0.5) and low (dashed line, budget level < 0.5) resource budget levels, illustrating how cue sensitivity is modulated by internal resource status. (B) GAM-smoothed surfaces of normalised seed production across the two-dimensional state space defined by weather cue (x-axis) and resource budget level (y-axis). Colours range from dark (low) to bright (high) normalised production.

In RB + WC, the pattern reversed markedly: the intercept dropped to 0.08, the lowest of all formulations, while the base rose to 6.74, implying a large increase in predicted allocation from WC = 0 to WC = 1 (from 0.08 to 0.54 on the normalised scale). This steep exponential indicates that the weather cue exerts a dominant influence on seed output in this formulation, with resource budget setting a threshold that cue intensity then amplifies. The heatmap reflects this structure: the allocation gradient intensifies more strongly along the cue axis than along the budget axis, and the lowest values are

confined to the low-cue region even when budget levels are high, confirming that favourable resource conditions are insufficient alone to trigger substantial seed production in RB+WC (Figure 6B).

In RB×WC, the multiplicative coupling between budget and cue introduced a budget-dependent sensitivity to cue intensity. Trees with high resource budget (≥ 0.5; $y = 0.32 \times 2.06^{WC}$) showed a higher intercept and a steeper rise with cue than those with low budget (< 0.5; $y = 0.18 \times 2.66^{WC}$), indicating that the cue signal is amplified when resources are available and attenuated when they are not. The heatmap illustrates this gating mechanism clearly: the highest allocation values are confined to the upper-right quadrant, where both budget level and cue intensity are simultaneously high, while neither condition alone produces the maximum response (Figure 6B). This joint dependency distinguishes RB×WC from the other formulations and aligns most closely with the prediction that masting requires the co-occurrence of sufficient energy reserves and an appropriate environmental signal.

3.4. Modelling masting under climate change

Observed CV_p remained elevated from the 1980–1990 period (~1.05) through the early 2000s, peaking at approximately 1.22 around 2005, before declining sharply to ~0.72 by 2020–2025 (Figure 7A). When averaged across all time windows, observed CV_p was 0.96. The RB formulation calibrated at the tree level consistently underestimated masting intensity throughout the series (mean $CV_p = 0.60$), while RB+WC most closely reproduced the observed mean (mean $CV_p = 0.99$) and RB×WC showed intermediate values (mean $CV_p = 0.71$; Supplementary Material S9).

Despite this ordering in mean performance, agreement between simulated and observed CV_p across time windows improved substantially with model complexity (Figure 7C). RB showed limited temporal correspondence ($R^2 = 0.30$), with simulated values confined to a narrow low range (~0.47–0.70) and no coherent tracking of the observed mid-period peak. RB+WC, despite reproducing the observed mean magnitude of interannual variability, did not consistently reproduce its temporal ordering ($R^2 = 0.12$), indicating that the additive weather cue shifts the average level of CV_p without reliably tracking its temporal modulation. The RB×WC formulation showed the strongest temporal agreement ($R^2 = 0.81$), correctly associating high-variability periods (2000–2010) with elevated simulated CV_p and the more recent windows (2020–2025) with lower values, though still underestimating absolute magnitudes.

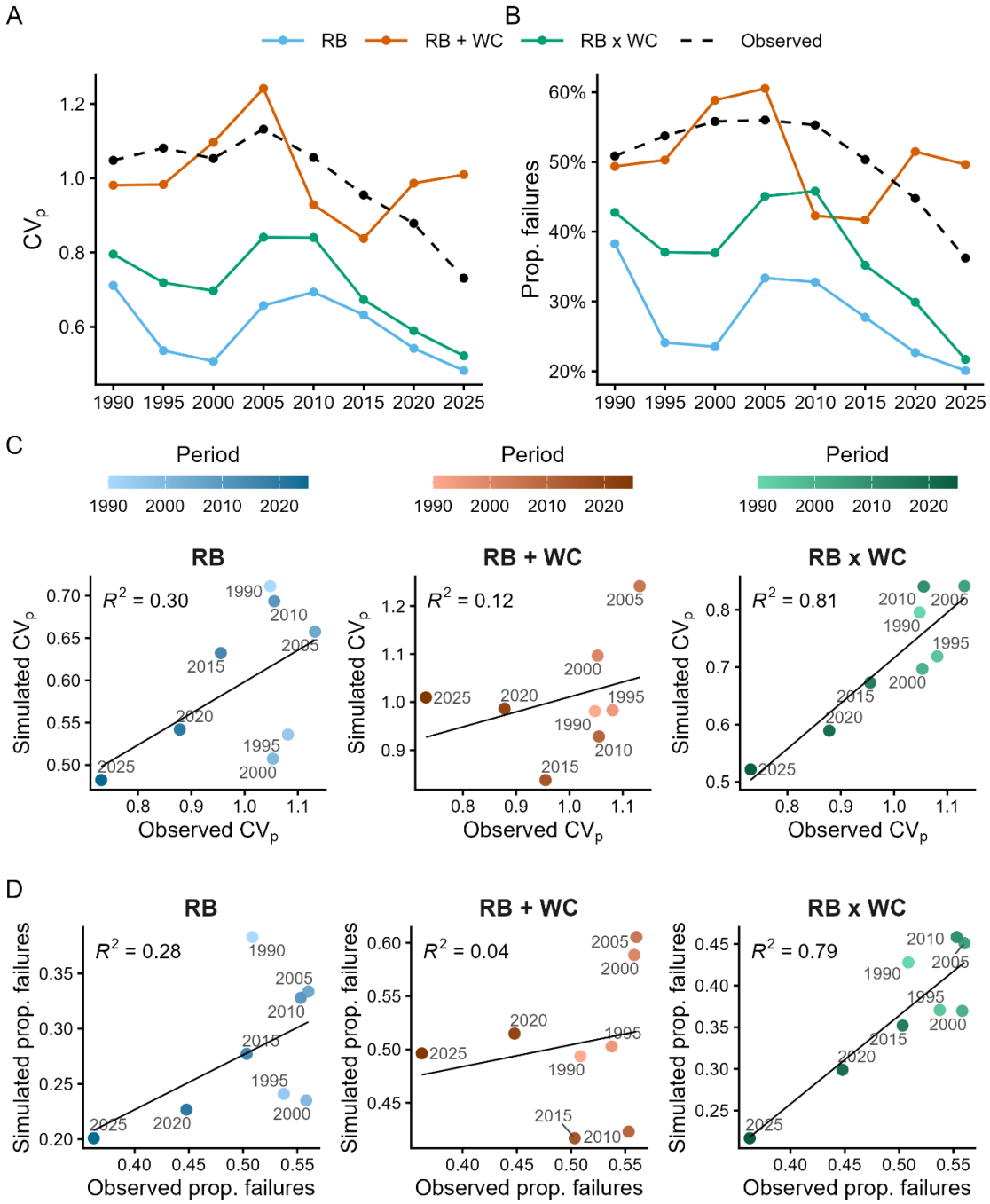

Figure 7. Temporal dynamics of masting intensity and reproductive failures across model formulations. (A) Observed and simulated masting intensity (CV_p, coefficient of variation of annual seed production) computed over 10-year moving windows with a 5-year step with models calibrated at the tree level; values are reported at the final year of each window (e.g., 1990 = 1980–1990). The black dashed line shows observed dynamics; coloured lines show simulations for the resource budget only (RB; blue), resource budget with additive weather cues (RB+WC; orange), and resource budget with multiplicative weather cues (RB×WC; green). (B) Observed and simulated proportion of reproductive failure years (normalised seed production < 0.25) over the same time windows. (C, D) Observed vs. simulated CV_p (C) and proportion of reproductive failures (D) across time windows for each formulation. Points represent individual time windows coloured from lighter (earlier) to darker (more recent) shades. Solid lines show fitted linear regressions; R^2 values are reported for each panel. Calibration metrics for country- and site-level parameterisations are reported in Table S9.

The proportion of reproductive failure years (defined as normalised seed production < 0.25) followed a broadly declining trend over the study period, from ~51% around 1990 to ~35% by 2020–2025 (Figure 7B). Mean observed failure frequency was 0.497. RB markedly underestimated reproductive failures (mean simulated failures = 0.272), RB+WC almost exactly reproduced the observed mean (failures = 0.496), and RB × WC showed intermediate performance (failures = 0.370). The pattern of temporal correspondence across windows closely mirrored that observed for CV_p (Figure 7D): RB showed modest but non-negligible tracking of the declining trend ($R^2 = 0.28$); RB+WC failed to reproduce the temporal ordering of failure rates ($R^2 = 0.04$); and RB×WC again provided the strongest agreement ($R^2 = 0.79$), correctly tracking the long-term reduction in failure frequency despite a persistent underestimation of its magnitude in recent windows. These results indicate that model performance on mean metrics and on temporal dynamics can diverge substantially: RB+WC best recovers average masting intensity and failure frequency, yet RB×WC is the only formulation that reliably tracks their temporal trajectories across changing climate conditions

3.5. Application: forecasting

We applied the three model versions in forecasting mode to generate site-level normalised seed production for 2023–2026 at 11 UK beech sites (Figure 8), after calibrating on 1980–2022 observational data. Forecasts were produced at three calibration levels: Country (a single parameter set shared across all sites), Site (site-specific parameters), and Tree (tree-specific parameters), to assess how parameterisation granularity influences forecast quality. Observations for 2025 were unavailable at two sites (Ripon and Spennymoor); no 2026 observations were available at any site at the time of writing, so simulated values for that year represent purely out-of-sample forecasts with no observational counterpart.

Forecast accuracy depended strongly on both model version and calibration level, though the two factors interacted differently across formulations (Figure 8, inset). At Country level, RB×WC achieved the lowest RMSE (0.27), outperforming both RB (0.37) and RB + WC (0.39), suggesting that the multiplicative cue mechanism provides a structural advantage when only coarse, regionally shared parameters are available. This advantage diminished as calibration granularity increased: at Site level, RB×WC RMSE rose to 0.31 (higher than both RB and RB + WC) before recovering to 0.25 at Tree level. By contrast, RB+WC showed the largest improvement with increasing calibration resolution, dropping from 0.39 (Country) to 0.25 (Tree). RB displayed the lowest overall Tree-level RMSE (0.23) and the smallest spread across calibration levels (0.23–0.37), indicating that its simpler structure is less sensitive to parameter specification and remains competitive at fine spatial resolution.

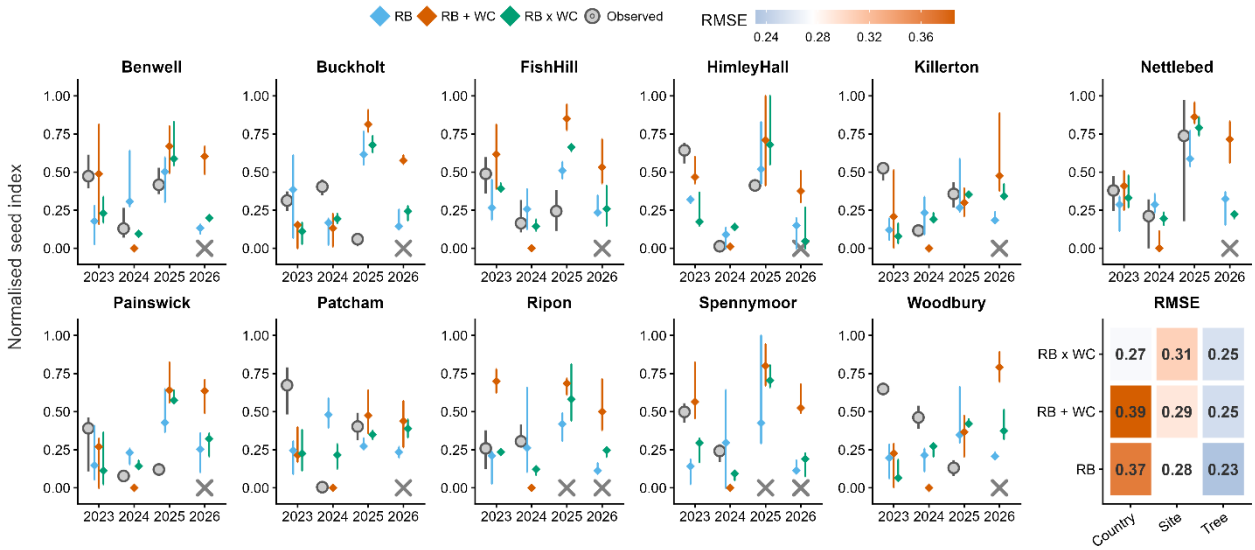

Figure 8. Site-level forecasts of normalised seed production for 2023–2026 across 11 UK beech sites. Grey symbols show the observed median normalised seed index per site and year, with vertical bars spanning the interquartile range (25th–75th percentile) across trees. Coloured symbols show simulated medians for three model versions — RB (blue), RB + WC (orange), and RB × WC (green) — with vertical bars indicating the interquartile range (25th–75th percentile) of simulated values pooled across three calibration levels (Country, Site, and Tree). All simulations were calibrated on 1980–2022 data only; the normalisation window matches this period. Outlier trees whose per-tree RMSE exceeded the Tukey fence (Q75 + 1.5 × IQR) were excluded prior to analysis. The inset heatmap shows RMSE between site–year simulated and observed medians for each combination of model version and calibration level; colour intensity indicates error magnitude (lighter = lower RMSE). Observations for 2025 were unavailable for Ripon and Spennymoor (×); no observations for 2026 were available at any site at the time of writing.

Forecast skill also varied markedly across years. The 2023 seed crop was generally well captured, with simulated medians close to observations at most sites. The 2024 low-production event was correctly identified by all formulations at several sites, including Benwell, Killerton, and Nettlebed, where forecast medians fell well below the normalised mean. In 2025, however, production was systematically overestimated: at sites where observed output remained low or moderate (e.g., Buckholt, Painswick, Patcham, Woodbury, Himley Hall, Fish Hill), simulated medians were substantially higher than observations across all model versions and calibration levels. This consistent positive bias, shared by every configuration, points to a structural limitation in the representation of multi-year low-production dynamics: the resource budget does not deplete sufficiently following consecutive poor seed years, generating positively biased predictions in the subsequent season.

For 2026, model forecasts diverged substantially across sites, with RB+WC projecting notably higher production than RB and RB×WC at several locations, most markedly at Spennymoor and Woodbury, where RB+WC medians approached or exceeded normalized value of 0.75 against values

of 0.05–0.30 for the other two formulations. This systematic spread suggests that the three model structures differ in how rapidly they anticipate resource recovery following consecutive years of low seed production.

4. Discussion

4.1. The mode of resource–cue integration drives model performance

Our study shows that a process-based model integrating resource dynamics and weather cues can reproduce key features of masting in European beech. The results reveal a finding more intricate than a simple complexity-performance hierarchy: the critical variable is not whether weather cues are incorporated, but how they are coupled to internal resource dynamics. The additive formulation (RB+WC) improved over the resource-budget-only model (RB) exclusively at country-level calibration (Figure 4C), but at finer calibration scales this advantage reversed: per-site R^2 at tree level was higher for RB (0.59) than for RB+WC (0.45), and the temporal correlation with observed annual seed production medians was likewise lower for RB+WC ($r = 0.76$) than for RB ($r = 0.86$; Figure 5B). Thus, incorporating a weather cue whose effect is independent of the resource state shifts the mean level of variability but disrupts the interannual timing of reproductive events when fine-scale calibration data are available. This pattern is consistent with the mast-seeding literature: weather cues are known to act as a large-scale synchronizing (Moran) signal shared by all individuals across a region (Koenig & Knops, 2013; Pearse et al., 2016), compensating for individual variability not yet captured by RB. This signal becomes misaligned, however, once individual variability is already well represented, as is the case at finer calibration levels, where the effect of weather cues on individual reproduction is instead scaled to the plant's internal resource state (Kelly et al., 2025). The RB×WC model, by letting weather modulate rather than simply add to the individual response, improved consistently across calibration levels, with the largest relative gains observed precisely at the finer scales (Figure 4A). The interactive formulation (RB×WC) is the only configuration that consistently improved performance across all dimensions: it achieved the highest temporal correlation ($r = 0.89$), the highest annual R^2 at tree level (0.82, Figure 4C), and the highest classification skill (quadratic-weighted $\kappa = 0.674$ at tree level; Table 2), confirming that the benefit of weather cues is strongest when cue sensitivity is gated by internal resource status (Monks *et al.*, 2016; Kelly *et al.*, 2025). Notably, the reduction in explained variance from tree- to country-level calibration was modest for RB×WC ($R^2 = 0.82$ to 0.68 at the annual scale, Figure 4C), indicating that the processes captured by this formulation are largely transferable across the observational network rather than site-specific.

Model performance was asymmetric across classes, with high-seeding years reproduced more closely than low-seeding years, an improvement over earlier forecasting models that struggled at both

ends of the distribution (Journé *et al.*, 2023a), but also an indication that the mechanisms producing very low seed crops remain incompletely represented (Oberklammer *et al.*, 2026).

The contrast between formulations clarifies how alternative resource–cue coupling structures generate these divergent outcomes. Even in the absence of an explicit cue mechanism, RB produced a shallow but real positive relationship between normalised seed production and weather cue intensity (Figure 6A), because warmer summers simultaneously enhance photosynthesis and resource accumulation and generate the temperature anomalies that serve as flowering cues in the other formulations. This emergent sensitivity indicates a covariance between resource state and cue conditions rather than an explicit cue effect and is consistent with the evolutionary argument that cue-driven masting may build on a pre-existing physiological sensitivity of reproduction to climatic variation, which selection then amplifies into a stronger, synchronised response (Janzen, 1971, 1976; Bogdziewicz *et al.*, 2020b). The shallow exponential base also explains why RB retains meaningful temporal skill ($r = 0.86$) despite underestimating mean masting intensity and failure frequency: the resource budget tracks real climatic variation, and the emergent cue covariance partially preserves interannual ordering. Adding weather cues additively steepened the response dramatically (Figure 6A), making seed output cue-dominated: production is near zero in cue-poor years regardless of resource status, while a strong cue can trigger substantial allocation even when the carbon budget is insufficient. This decoupling from internal resource state explains the behavior of RB+WC: it recovers the observed mean level of interannual variability but loses the temporal ordering of mast and failure years ($r = 0.76$, the lowest of all formulations; Figure 5B), because cue-driven variability is statistically plausible in aggregate but temporally misaligned with the specific year-by-year combination of resource state and cue intensity that determines real masting events. The multiplicative formulation resolved this tension: high-budget trees (≥ 0.5) showed a higher baseline allocation amplified by a moderate cue response ($y = 0.32 \times 2.06^{WC}$), while low-budget trees started from a lower baseline but were proportionally more sensitive to cue variation ($y = 0.18 \times 2.66^{WC}$; Figure 6A). The net result, i.e., high-budget trees always produce more at any given cue level, while resource-limited trees show a steeper relative response, generates the joint allocation surface in which maximum seed production requires the co-occurrence of both favourable cue conditions and sufficient reserves (Figure 6B), the structure most consistent with theoretical predictions that masting depends on both resource matching and cue sensitivity (Kelly, 1994; Kelly *et al.*, 2025). RB+WC per-class performance further illustrates this distinction: it substantially increased failure-year detection (POD 71% vs. 47% for RB) but reduced accuracy for intermediate classes; RB×WC achieved a more balanced improvement (failure detection 64%, mast-year detection 54% vs. 48% for RB+WC), discriminating at both extremes without degrading intermediate categories (Figure 5A).

4.2. Parameter calibration and sensitivity

Rather than treating all physiologically relevant parameters as free, we fixed respiration-related parameters, i.e., maintenance respiration rates for wood and leaves, and the Q_{10} temperature coefficient at plausible values for temperate broadleaved trees (Running & Hunt, 1993; Damesin, 2003). Although the Morris sensitivity analysis confirmed that these parameters contribute meaningfully to the carbon budget, their temperature-response relationships are well-constrained by independent process-level measurements and including them as free calibration parameters would introduce degrees of freedom without a corresponding gain in interpretability. Light use efficiency (LUE) was therefore retained as the single integrated parameter governing net carbon assimilation, and emerged as the dominant control on mean carbon allocated to seeds with predominantly linear and additive effects on carbon assimilation (Figure 3A–B). Calibrated LUE ranged from 1.42 to 1.87 g DM MJ^{-1} across sites and calibration levels, consistent with values reported for temperate broadleaved species (Yuan *et al.*, 2007; Liu *et al.*, 2022).

Phenological parameters were anchored to observable biological thresholds. The ecodormancy photothermal threshold (ECO), governing the transition from endodormancy to ecodormancy, ranged from 2 to 11 days of photothermal accumulation, within the range estimated from MODIS NDVI phenology across UK beech sites (Bajocco *et al.*, 2025). Flowering time (FLO_t) was concentrated in the first 3–8% of the growth phase, consistent with the spring flowering phenology of *Fagus sylvatica* (Gömöry & Paule, 2011), and flowering duration (FLO_d) showed limited variability across calibration levels, reflecting the species' narrow window of pollen viability (Bogdziewicz *et al.*, 2017). The pollination precipitation limit (POL_p) ranged from 5 to 14 mm, defining the daily rainfall threshold above which pollination success is substantially reduced.

Reproductive allocation parameters showed the broadest sensitivity to calibration scale. The flower-to-fruit cost (FFC, 0.18 – 0.29) represents the carbon expenditure per flower successfully converted to a ripe seed; it was parameterised by inverting the fruit-to-flower ratios reported for *Fagus sylvatica* (Isagi *et al.*, 1997), which classically express the fraction of female flowers developing into viable seeds, recasting this relationship as a per-unit reproductive cost more directly tractable within a carbon-budget framework. The reproduction threshold (REP_{thr}) ranged from 0.45 to 0.65, with higher values at tree level reflecting individual variation in the minimum resource level required to initiate significant seed production. REP_{thr} was the leading driver of interannual variability in seed production, yet nearly irrelevant for mean production (Figure 3C–D): by defining the binary threshold below which no reproductive investment occurs, it amplifies year-to-year contrasts without altering long-term carbon means. Its influence on interannual CV was strongly formulation-dependent: highest in RB, where it acts exclusively through the budget level; intermediate in RB×WC, where the

Gompertz cue-response partially decouples variability from the carbon scale; and weakest in RB+WC, where the additive cue asymptote allows reproductive investment even when the budget threshold is not crossed.

4.3. Calibration scale and forecasting skills

The model also showed useful short-term forecasting skill. When calibrated on 1980–2022 data and projected forward without recalibration, it reproduced broad year-to-year variation in seed production during 2023–2026 and some among-site differences in crop size. The 2023 seed crop was generally well captured, and the 2024 low-production event was correctly identified by all formulations at several sites including Benwell, Killerton, and Nettlebed, where forecast medians fell clearly below average. By contrast, the 2025 crop was systematically overestimated across all model versions, calibration levels, and sites: at sites where observed production remained low or moderate (e.g., Buckholt, Painswick, Patcham, Woodbury, HimleyHall, FishHill), predicted values were substantially higher than observations. This consistent overestimation is the operational manifestation of the structural limitation identified in the long-term analysis: the resource budget recovers too readily after a poor seed year, preventing the carry-over depletion that sustained low production across consecutive seasons. The model thus captures broad interannual variation better than it predicts the exact magnitude of low or multi-year poor crops, a pattern consistent with the broader challenge in mast forecasting of predicting extreme outcomes (Journé *et al.*, 2023a; Wion *et al.*, 2025). Even so, forecasts that correctly identify the direction of interannual change have clear operational value (Pearse *et al.*, 2021; Oberklammer *et al.*, 2026): anticipating productive years can support seed collection, nursery planning, and staff allocation, and identifying likely poor years can guide game management and avoid unnecessary organisational investment (Bisi *et al.*, 2018).

The three calibration levels reveal an interaction between model structure and data availability that carries direct implications for operational use (Figure 8; Table 2). Classification skill improved consistently from country to tree level for all formulations, and RB×WC retained the largest advantage across all scales. The forecast RMSE pattern was more complex, however. At country level, where a single parameter set represents the entire species, RB×WC achieved the lowest RMSE (0.27), outperforming RB (0.37) and RB+WC (0.40): the multiplicative gating of cue sensitivity by resource status provides structural robustness when parameterisation cannot be tailored to local conditions, compensating architecturally for what cannot be compensated parametrically. This advantage did not persist as calibration granularity increased: at site level, RB×WC RMSE rose to 0.32, higher than both RB (0.28) and RB+WC (0.29), before recovering to 0.26 at tree level, where it is matched by RB+WC. The lowest overall forecast RMSE was achieved by RB at tree level (0.23).

The non-monotonic behaviour of RB×WC across calibration scales suggests that site-level calibration introduces equifinality that the multiplicative structure is particularly susceptible to, while individual-tree tuning resolves this by anchoring parameters to observed individual-level variation. These results indicate that RB×WC is the formulation of choice when only regional or species-wide parameterisation is available, and also whenever classification skill is the primary objective; the simpler formulations remain competitive for point-forecast accuracy when individual-tree monitoring data allow fine-grained recalibration. The decline in performance from tree to country level is not a statistical artefact of pooling but quantifies what is genuinely gained by investing in site-specific or individual-tree monitoring.

4.4. Mechanistic interpretation and future directions

Beyond predictive performance, MASTHING provides a conceptual advance over purely statistical approaches by explicitly tracking the physiological pathways linking weather, phenology, carbon balance, and reproduction. The global sensitivity analysis confirmed that the dominant sources of variability in mean seed production and its interannual dynamics operate through contrasting mechanisms, providing independent, mechanistic support for the parameter selection strategy and making the models behaviour interpretable in terms of specific biological processes. Because the model resolves resource dynamics at daily resolution, individual mechanisms can be modified or suppressed in isolation, enabling hypothesis-testing uses that are not possible with statistical models. The comparison among formulations here is itself an example: the contrasting response surfaces in Figure 6 directly illustrate how alternative assumptions about resource–cue coupling translate into different predictions, and the CV_p analysis (Figure 7) identifies the long-term decline in interannual variability as the specific aspect of masting dynamics that current formulations fail to capture quantitatively and that future refinements should target. A particular strength of the framework is the coupling of reproduction to canopy phenology, which controls the seasonal timing of carbon acquisition and reproductive decisions. In the current implementation, weather cues are evaluated within a fixed post-solstice window (Journé *et al.*, 2024), but the model structure would also allow cue perception to be linked directly to phenological development, potentially improving the representation of state-dependent cue expression and helping to explain both extreme mast years and the long-term changes documented here and elsewhere (Foest *et al.*, 2024, 2025; Jantzen *et al.*, 2026). Because the model is parsimonious in input requirements and transferable through recalibration, MASTHING also provides a flexible framework for extending this approach to other masting species.

5. Conclusions

We developed MASTHING, a process-based model integrating phenology-driven resource acquisition, a dynamic resource budget, temperature-based flowering cues, and environmental vetoes during pollination and seed ripening. The central finding is that the mode of resource-cue integration is decisive: a multiplicative, resource-gated coupling is the only formulation that simultaneously improves classification skill, temporal correlation, and structural robustness across all calibration scales, whereas an additive coupling recovers the observed mean level of masting intensity but degrades temporal performance when fine-scale calibration data are available. By resolving carbon dynamics at daily resolution and linking them explicitly to phenology and reproduction, MASTHING provides a transparent platform for testing mechanistic hypotheses about resource–climate coupling and for generating useful short-term forecasts, including the correct identification of the 2024 low-production event at multiple UK sites. The systematic overestimation of the 2025 crop and the underestimation of the long-term CV_p decline point to the insufficient carry-over depletion after consecutive poor seed years, which is a clear target for future refinement. The results demonstrate that a process-based framework can advance both mechanistic understanding and operational forecasting of masting under climate change, and quantify precisely what is gained and what remains to be improved in its representation.

Acknowledgements

This study was funded by the Italian Ministry of Agriculture, Food Sovereignty and Forestry (MASAF, SOFIA, DM 0656382), by Ferrero Trading Lux (HAZIMUT project), and by the European Union (ERC, ForestFuture, 101039066). Views and opinions expressed are, however, those of the authors only and do not necessarily reflect those of the European Union or the European Research Council. Neither the European Union nor the granting authority can be held responsible for them. AI tools (Claude, Chat-GPT) were used to improve the clarity and readability of portions of this manuscript. All scientific content, analyses, and interpretations remain entirely the work of the authors, who take full responsibility for the accuracy of the information presented.

Author Contributions Statement

Simone Bregaglio: Conceptualization, Methodology, Software, Formal analysis, Visualization, Writing – original draft. Sofia Bajocco: Conceptualization, Methodology, Writing – review & editing. Carlotta Ferrara: Conceptualization, Methodology, Writing – review & editing. Michał Bogdziewicz: Conceptualization, Methodology, Data curation, Writing – original draft, review & editing. Andrew Hacket-Pain: Conceptualization, Methodology, Data curation, Writing – original

draft, review & editing. Francesco Chianucci: Project administration, Conceptualization, Methodology, Formal analysis, Visualization, Writing – original draft, review & editing.

Declaration of interests

No competing interests to declare.

Data and code availability statement

The data that support the findings of this study are available upon request from dr. Andrew Hacket-Pain. Data requests should be addressed to andrew.hacket-pain@liverpool.ac.uk. The MASTHING source code is openly available at https://github.com/GeoModelLab/MASTHING and archived on Zenodo (https://doi.org/10.5281/zenodo.19660460).

References

Asse, D., Randin, C.F., Bonhomme, M., Delestrade, A., Chuine, I., 2020. Process-based models outcompete correlative models in projecting spring phenology of trees in a future warmer climate. *Agricultural and Forest Meteorology* 285–286, 107931. https://doi.org/10.1016/j.agrformet.2020.107931

Barczyk, M.K., Bogdziewicz, M., Drobniak, S.M., Bogdańska, M., Eichert, U., Foest, J.J., Journe, V., Kondrat, K., Szymkowiak, J., Hacket-Pain, A., 2026. Growth–reproduction trade-offs are common but changing in woody plants: a meta-analysis. *EcoEvoRxiv* https://doi.org/10.32942/X2966R

Bajocco, S., Ricotta, C., Bregaglio, S., 2025. Bridging the gap between remotely sensed phenology and the underlying ecophysiological processes: The SWELL model. *Methods in Ecology and Evolution*, 16, 1473–1488. https://doi.org/10.1111/2041-210X.70067

Bartelink, H.H., 1997. Allometric relationships for biomass and leaf area of beech (*Fagus sylvatica* L.). *Annales des sciences forestières*, 54, 39–50. https://doi.org/10.1051/forest:19970104

Bisi, F., Chirichella, R., Chianucci, F., Von Hardenberg, J., Cutini, A., Martinoli, A., Apollonio, A., 2018. Climate, tree masting and spatial behaviour in wild boar (*Sus scrofa* L.): insight from a long-term study. *Annals of Forest Science*, 75, 46. https://doi.org/10.1007/s13595-018-0726-6

Bogdziewicz, M., Szymkowiak, J., Kasprzyk, I., Grewling, Ł., Borowski, Z., Borycka, K., Kantorowicz, W., Myszkowska, D., Piotrowicz, K., Ziemianin, M., Pesendorfer, M.B., 2017. Masting in wind-pollinated trees: system-specific roles of weather and pollination dynamics in driving seed production. *Ecology* 98, 2615–2625. https://doi.org/10.1002/ecy.1951

Bogdziewicz, M., Steele, M., Marino, S., Crone, E., 2018. Correlated seed failure as an environmental veto to synchronize reproduction of masting plants. *New Phytologist* 219, 98–108. https://doi.org/10.1111/nph.15108

Bogdziewicz, M., Ascoli, D., Hacket-Pain, A., Koenig, W.D., Pearse, I., Pesendorfer, M., Satake, A., Thomas, P., Vacchiano, G., Wohlgemuth, T., Tanentzap, A., 2020a. From theory to experiments for testing the proximate mechanisms of mast seeding: an agenda for an experimental ecology. *Ecology Letters* 23, 210–220. https://doi.org/10.1111/ele.13442

Bogdziewicz, M., Kelly, D., Tanentzap, A.J., Thomas, P.A., Lageard, J.G., Hacket-Pain, A., 2020b. Climate change strengthens selection for mast seeding in European beech. *Current Biology* 30, 3477–3483.e2. https://doi.org/10.1016/j.cub.2020.06.056

Bogdziewicz, M., Kelly, D., Thomas, P.A., Lageard, J.G.A., Hacket-Pain, A., 2020c. Climate warming disrupts mast seeding and its fitness benefits in European beech. *Nature Plants* 6, 88–94. https://doi.org/10.1038/s41477-020-0592-8

Bogdziewicz, M., Hacket-Pain, A., Kelly, D., Thomas, P.A., Lageard, J., Tanentzap, A.J., 2021. Climate warming causes mast seeding to break down by reducing sensitivity to weather cues. *Global Change Biology* 27, 1952–1961. https://doi.org/10.1111/gcb.15560

Bogdziewicz, M., Kelly, D., Tanentzap, A.J., Thomas, P., Foest, J., Lageard, J., Hacket-Pain, A., 2023. Reproductive collapse in European beech results from declining pollination efficiency in large trees. *Global Change Biology*, 29, 4595–4604. https://doi.org/10.1111/gcb.16730

Bogdziewicz, M., Kelly, D., Ascoli, D., Caignard, T., Chianucci, F., Crone, E.E., Fleurot, E., Foest, J.J., Gratzer, G., Hagiwara, T., Han, Q., Journé, V., Keurinck, L., Kondrat, K., McClory, R., LaMontagne, J.M., Mundo, I.A., Nussbaumer, Oberklammer, I., Ohno, M., Pearse, I.S., Pesendorfer, M.B., Resente, G., Satake, A., Shibata, M., Snell, R.S., Szymkowiak, J., Touzot, L., Zwolak, R., Zywiec, M., Hacket-Pain, A., 2024. Evolutionary ecology of masting: mechanisms, models, and climate change. *Trends in Ecology & Evolution* 39, 851–862. https://doi.org/10.1016/j.tree.2024.05.006

Bregaglio, S., Ginaldi, F., Raparelli, E., Fila, G., Bajocco, S., 2023. Improving crop yield prediction accuracy by embedding phenological heterogeneity into model parameter sets. *Agricultural Systems* 209, 103666. https://doi.org/10.1016/j.agsy.2023.103666

Bregaglio, S., Bajocco, S., Ferrara, C., Bogdziewicz, M., Hacket-Pain, A., & Chianucci, F. (2026). MASTHING: a process-based model of mast seeding in European beech (Version 1.0.0) [Computer software]. *Zenodo*. https://doi.org/10.5281/zenodo.19660460

Briscoe, N.J., Morris, S.D., Mathewson, P.D., Buckley, L.B., Jusup, M., Levy, O., Maclean, I.M.D., Pincebourde, S., Riddell, E.A., Roberts, J.A., Schouten, R., Sears, M.W., Kearney, M.R., 2023.

Mechanistic forecasts of species responses to climate change: The promise of biophysical ecology. *Global Change Biology* 29, 1451–1470. https://doi.org/10.1111/gcb.16557.

Campolongo, F., Cariboni, J., Saltelli, A., 2007. An effective screening design for sensitivity analysis of large models. *Environmental Modelling & Software* 22, 1509–1518. https://doi.org/10.1016/j.envsoft.2006.10.004

Clark, J.S., Nuñez, C., Tomasek, B., 2019. Foodwebs based on unreliable foundations: spatiotemporal masting merged with consumer movement, storage, and diet. *Ecological Monographs* 89, e01381. https://doi.org/10.1002/ecm.1381

Crone, E.E., Rapp, J.M., 2014. Resource depletion, pollen coupling, and the ecology of mast seeding. *Annals of the New York Academy of Sciences* 1322, 21–34. https://doi.org/10.1111/nyas.12465

Damesin, C., 2003. Respiration and photosynthesis characteristics of current-year stems of Fagus sylvatica: from the seasonal pattern to an annual balance. *New Phytologist* 158, 465–475. https://doi.org/10.1046/j.1469-8137.2003.00756.x

Elliott, G., Kemp, J., 2016. Large-scale pest control in New Zealand beech forests. *Ecological Management and Restoration* 17, 200–209. https://doi.org/10.1111/emr.12227

Fernández-Martínez, M., Bogdziewicz, M., Espelta, J.M., Peñuelas, J., 2017. Nature beyond linearity: Meteorological variability and jensen's inequality can explain mast seeding behaviour. *Frontiers in Ecology and Evolution* 5, 134. https://doi.org/10.3389/fevo.2017.00134

Fibbi, L., Moriondo, M., Chiesi, M., Bindi, M., Maselli, F., 2019. Impacts of climate change on the gross primary production of Italian forests. *Annals of Forest Science* 76, 59. https://doi.org/10.1007/s13595-019-0843-x

Foest, J.J., Bogdziewicz, M., Pesendorfer, M.B., Ascoli, D., Cutini, A., Nussbaumer, A., Verstraeten, A., Beudert, B., Chianucci, F., Mezzavilla, F., Gratzer, G., Kunstler, G., Meesenburg, H., Wagner, M., Mund, M., Cools, N., Vacek, S., Schmidt, W., Vacek, Z., Hacket-Pain, A., 2024. Widespread breakdown in masting in European beech due to rising summer temperatures. *Global Change Biology* 30, e17307. https://doi.org/10.1111/gcb.17307

Foest, J.J., Szymkowiak, J., Dyderski, M.K., Jastrzębowski, S., Fuchs, H., Ratajczak, E., Hacket-Pain, A., Bogdziewicz M., 2025. No Refuge at the Edge for European Beech as Climate Warming Disproportionately Reduces Masting at Colder Margins. *Ecology Letters* 28, e70284. https://doi.org/10.1111/ele.70284.

Forrester, D., Tachauer, I., Annighoefer, P., Barbeito, I., Pretzsch, H., Ruiz-Peinado, R., Stark, H., Vacchiano, G., Zlatanov, T., Chakraborty, T., Saha, S., Sileshi, G.W., 2017. Generalized biomass and leaf area allometric equations for European tree species incorporating stand structure, tree age and

climate. *Forest Ecology and Management* 396, 160–175. https://doi.org/10.1016/j.foreco.2017.04.011.

Gömöry, D., Paule, L., 2011. Trade-off between height growth and spring flushing in common beech (*Fagus sylvatica* L.). *Annals of Forest Science* 68, 975–984. https://doi.org/10.1007/s13595-011-0103-1.

Gorelick, N., Hancher, M., Dixon, M., Ilyushchenko, S., Thau, D., Moore, R., 2017. Google Earth Engine: Planetary-scale geospatial analysis for everyone. *Remote Sensing of Environment* 202, 18–27, https://doi.org/10.1016/j.rse.2017.06.031.

Hacket-Pain, A., Bogdziewicz, M., 2021. Climate change and plant reproduction: trends and drivers of mast seeding change. *Philosophical Transactions of the Royal Society B* 376, 20200379. https://doi.org/10.1098/rstb.2020.0379

Hacket-Pain, A., Szymkowiak, J., Journé, V., Barczyk, M.K., Thomas, P.A., Lageard, J.G.A., Kelly, D., Bogdziewicz, M., 2025. Growth decline in European beech associated with temperature-driven increase in reproductive allocation. *Proceedings of the National Academy of Sciences* 122, e2423181122. https://doi.org/10.1073/pnas.2423181122

Hargreaves, G.H., Samani, Z.A., 1985. Reference crop evapotranspiration from temperature. *Applied Engineering in Agriculture* 1, 96–99. http://dx.doi.org/10.13031/2013.26773

Hauck, M., Schneider, T., Bahlinger, S., Fischbach, J., Oswald, G., Csapek, G., Dulamsuren, C., 2025. Heat tolerance of temperate tree species from Central Europe. *Forest Ecology and Management* 580, 122541. https://doi.org/10.1016/j.foreco.2025.122541.

Hirsch, M., Puhlmann, H., Klemmt, H.J., Seifert, T., 2025. Modelling fructification intensity at the tree level reveals species-specific effects of tree age, social status and crown defoliation across major European tree species. *European Journal of Forest Research* 144, 1505–1522. https://doi.org/10.1007/s10342-025-01822-0.

Holben, B.N., 1986. Characteristics of maximum-value composite images from temporal AVHRR data. *International Journal of Remote Sensing*, 7, 1417–1434. https://doi.org/10.1080/01431168608948945

Hufkens, K., 2023. The MODISTools package: an interface to the MODIS Land Products Subsets Web Services. doi:10.5281/zenodo.7551165, https://doi.org/10.5281/zenodo.7551165.

Iooss, B., Da Veiga, S., Janon, A., Pujol, G., 2026. sensitivity: Global Sensitivity Analysis of Model Outputs and Importance Measures. R package version 1.31.0, https://CRAN.R-project.org/package=sensitivity.

Isagi, Y., Sugimura, K., Sumida, A., Ito, H., 1997. How does masting happen and synchronize? *Journal of Theoretical Biology* 187, 231–239. https://doi.org/10.1006/jtbi.1997.0442

Jantzen, C., Burant, J., Gamelon, M., Bakker, E.L., Visser, M.E., 2026. Masting breakdown in European beech reduces fitness benefits of masting, partly explained by climate change. Ecology and Evolution 16, e73809. https://doi.org/10.1002/ece3.73809

Janzen, D.H., 1971. Seed predation by animals. *Annual Review of Ecology and Systematics*, 220, 465–492. https://doi.org/10.1146/annurev.es.02.110171.002341

Janzen, D.H., 1976. Why bamboos wait so long to flower. *Annual Review of Ecology and Systematics*, 7, 347–391. https://doi.org/10.1146/annurev.es.07.110176.002023

Journé, V., Hacket-Pain, A., Bogdziewicz, M., 2023a. Evolution of masting in plants is linked to investment in low tissue mortality. *Nature Communications*, 14, 7998. https://doi.org/10.1038/s41467-023-43616-1

Journé, V., Hacket-Pain, A., Oberklammer, I., Pesendorfer, M.B., Bogdziewicz, M., 2023b. Forecasting seed production in perennial plants: identifying challenges and charting a path forward. *New Phytologist* 239, 466–476. https://doi.org/10.1111/nph.18957

Journé, V., Szymkowiak, J., Foest, J., Hacket-Pain, A., Kelly, D., Bogdziewicz, M., 2024. Summer solstice orchestrates the subcontinental-scale synchrony of mast seeding. *Nature Plants* 10, 367–373. https://doi.org/10.1038/s41477-024-01651-w

Kabeya D, Iio A, Kakubari Y, Han Q., 2021. Dynamics of non-structural carbohydrates following a full masting event reveal a role for stored starch in relation to reproduction in *Fagus crenata*. *Forest Research (Fayettev)* 1, 18. https://doi.org/10.48130/FR-2021-0018

Kelly, D., 1994. The evolutionary ecology of mast seeding. *Trends in Ecology Evolution* 9, 465–470. https://doi.org/10.1016/0169-5347(94)90310-7

Kelly, D., Geldenhuis, A., James, A., Holland, E.P., Plank, M.J., Brockie, R.E., Cowan, P.E., Harper, G.A., Lee, G.W., Maitland, M.J., Mark, A.F., Mills, J.A., Wilson, P.R., Byrom, A.E., 2013. Of mast and mean: differential-temperature cue makes mast seeding insensitive to climate change. *Ecology Letters* 16, 90–98. https://doi.org/10.1111/ele.12020

Kelly, D., Hart, D.E., Allen, R.B., 2001. Evaluating the wind pollination benefits of mast seeding. *Ecology*, 82, 117–126. https://doi.org/10.1890/0012-9658(2001)082[0117:ETWPBO]2.0.CO;2

Kelly, D., Sork, V.L., 2002. Mast seeding in perennial plants: Why, how, where? *Annual Review of Ecology and Systematics* 33, 427–447. https://doi.org/10.1146/annurev.ecolsys.33.020602.095433

Kelly, D., Szymkowiak, J., Hacket-Pain, A., Bogdziewicz, M., 2025. Fine-tuning mast seeding: as resources accumulate, plants become more sensitive to weather cues. *New Phytologist* 246, 1975–1985. https://doi.org/10.1111/nph.70092

Koenig, W.D., Knops, J.M.H., 2013. Large-scale spatial synchrony and cross-synchrony in acorn production by two California oaks. *Ecology* 94, 83–93. https://doi.org/10.1890/12-0940.1

Lin, Y.S., Medlyn, B.E., Ellsworth, D.S., 2012. Temperature responses of leaf net photosynthesis: the role of component processes. *Tree Physiology* 32, 219–231. https://doi.org/10.1093/treephys/tpr141

Liu, L., Gao, X., Cao, B., Ba, Y., Chen, J., Cheng, X., Zhou, Y., Huang, H., Zhang, J., 2022. Comparing Different Light Use Efficiency Models to Estimate the Gross Primary Productivity of a Cork Oak Plantation in Northern China. *Remote Sensing* 14, 5905. https://doi.org/10.3390/rs14225905

Maselli, F., Chiesi, M., Angeli, L., Fibbi, L., Rapi, B., Romani, M., Sabatini, F., Battista, B., 2020. An improved NDVI-based method to predict actual evapotranspiration of irrigated grasses and crops. *Agricultural Water Management* 233, 106077. https://doi.org/10.1016/j.agwat.2020.106077

Medlyn, B.E., 1998. Physiological basis of the light use efficiency mode. *Tree Physiology*, 18, 167–176. https://doi.org/10.1093/treephys/18.3.167

Monks, A., Monks, J.M., Tanentzap, A.J., 2016. Resource limitation underlying multiple masting models makes mast seeding sensitive to future climate change. *New Phytologist*, 210, 419–430. https://doi.org/10.1111/nph.13817

Monteith, J.L., 1972. Solar radiation and productivity in tropical ecosystems. *Journal of Applied Ecology* 9, 747–766. https://doi.org/10.2307/2401901

Morris, M.D., 1991. Factorial sampling plans for preliminary computational experiments. *Technometrics* 33, 161–174. https://doi.org/10.1080/00401706.1991.10484804

Mäkelä, A., Landsberg, J., Ek, A.R., Burk, T.E., Ter-Mikaelian, M., Ågren, G.I., Oliver, C.D., Puttonen, P., 2000. Process-based models for forest ecosystem management: current state of the art and challenges for practical implementation. *Tree Physiology* 20, 289–298. https://doi.org/10.1093/treephys/20.5-6.289

Oberklammer, I., Gratzer, G., Schueler, S., Konrad, H., Hacket-Pain, A., Pesenforfer, M.B., 2026. See(d)ing the seeds - toward weather-based forecasting of annual seed production in six European forest tree species. *EcoEvoRxiv*. https://doi.org/10.32942/X2T05Z

Ostfeld, R.S., LaDeau, S.L., Oggenfuss, K., Canham, C.D., Fargione, M., Winchcombe, R.J., Keesing, F., 2026. The ecology of Lyme disease: Long-term data, surprises, and a synthesis. *Proceedings of the National Academy of Science U.S.A.* 123, e2610907123. https://doi.org/10.1073/pnas.261090712

Packham, J.R., Thomas, P.A., Lageard, J.G., Hilton, G.M., 2008. The English beech masting survey 1980–2007: Variation in the fruiting of the common beech (*Fagus sylvatica* L.) and its effects on woodland ecosystems. *Arboricultural Journal* 31, 189–214. https://doi.org/10.1080/03071375.2008.9747535

Pearse, I.S., Koenig, W.D., Kelly, D., 2016. Mechanisms of mast seeding: resources, weather, cues, and selection. *New Phytologist* 212, 546–562. https://doi.org/10.1111/nph.14114

Pearse, I.S., Wion, A.P., Gonzalez, A.D., Pesendorfer, M.B., 2021. Understanding mast seeding for conservation and land management. *Philosophical Transactions of the Royal Society B: Biological Sciences* 376, 34657466. https://doi.org/10.1098/rstb.2020.0383

Penning de Vries, F.W.T., Jansen, D.M., tenBerge, H.F.M., Bakema, A., 1989. Simulation of ecophysiological processes of growth in several annual crops. Pudoc; IRRI

Rapp, J.M., Mcintire, E.J., Crone, E.E., 2013. Sex allocation, pollen limitation and masting in whitebark pine. *Journal of Ecology* 101, 1345–1352. https://doi.org/10.1111/1365-2745.12115

Roncé, I.L., Dardevet, E., Venner, S., Schönbeck, L., Gessler, A., Chuine, I., Limousin, J.M., 2023. Reproduction alternation in trees: testing the resource depletion hypothesis using experimental fruit removal in *Quercus ilex*. *Tree Physiology* 43, 952–964. https://doi.org/10.1093/treephys/tpad025

Running, S.W., Hunt, E.R., 1993. Generalization of a Forest Ecosystem Process Model for Other Biomes, BIOME-BGC, and an Application for Global-Scale Models. In: Physiological Ecology, Scaling Physiological Processes, Academic Press, Pages 141-158. https://doi.org/10.1016/B978-0-12-233440-5.50014-2.

Sala, A., Hopping, K., McIntire, E.J., Delzon, S., Crone, E.E., 2012. Masting in whitebark pine (*Pinus albicaulis*) depletes stored nutrients. *New Phytologist* 196, 189–199. https://doi.org/10.1111/j.1469-8137.2012.04257.x

Satake, A., Journé, V., 2026. Linking gene regulation to flowering phenology under climate change: a dynamical modelling approach. *Contemporary Physics* 67, 3–13. https://doi.org/10.1080/00107514.2026.2613595

Smaill, S.J., Clinton, P.W., Allen, R.B., Davis, M.R., 2011. Climate cues and resources interact to determine seed production by a masting species. *Journal of Ecology*, 99, 870–877. https://doi.org/10.1111/j.1365-2745.2011.01803.x

Sofiev, M., Siljamo, P., Ranta, H., Linkosalo, T., Jaeger, S., Rasmussen, A., Rantio-Lehtimaki, A., Severova, E., Kukkonen, J., 2013. A numerical model of birch pollen emission and dispersion in the atmosphere. description of the emission module. *International Journal of Biometeorology* 57, 45–58. https://doi.org/10.1007/s00484-012-0532-z

Tattoni, C., Corradini, A., Chianucci, F., Ciolli, M., Giusti, R., Bragalanti, N., Cagnacci, F., Martinoli, A., Preatoni, D.G., Bisi, F., 2025. Behaviour of brown bears under fluctuating resource availability. *Ecology and Evolution* 15, e71693. https://doi.org/10.1002/ece3.71693

Vacchiano, G., Hacket-Pain, A., Turco, M., Motta, R., Maringer, J., Conedera, M., Drobyshev, I., Ascoli, D., 2017. Spatial patterns and broad-scale weather cues of beech mast seeding in Europe. *New Phytologist* 215, 595–608. https://doi.org/10.1111/nph.14600

Vacchiano, G., Ascoli, D., Berzaghi, F., Lucas-Borja, M.E., Caignard, T., Collalti, A., Mairota, P., Palaghianu, C., Reyer, C.P.O., Sanders, T.G.M., Schermer, E., Wohlgemuth, T., Hacket-Pain, A., 2018. Reproducing reproduction: How to simulate mast seeding in forest models. *Ecological Modelling*, 376, 40–53. https://doi.org/10.1016/j.ecolmodel.2018.03.004

Végh, L., Kato, T., 2024. Modified SEIB-DGVM enables simulation of masting in a temperate forest. *Ecological Modelling*, 488, 110577. https://doi.org/10.1016/j.ecolmodel.2023.110577

Vitasse, Y., Spafford, L., Reim, J., Baumgarten, F., Martínez-Sancho, E., 2025. Emerging trend of increasing spring frost damage for beech at higher elevations in the Jura Mountains: evidence from tree-ring data. *New Phytologist* 248, 600–614. https://doi.org/10.1111/nph.70471

Wion, A.P., Pearse, I.S., Broxson, M., Redmond, M.D., 2025. Mast hindcasts reveal pervasive effects of extreme drought on a foundational conifer species. *New Phytologist*, 246, 450–460. https://doi.org/10.1111/nph.20321

Yeoh, S.H., Satake, A., Numata, S., Ichie, T., Lee, S.L., Basherudin, N. *et al.* (2017). Unravelling proximate cues of mass flowering in the tropical forests of South-East Asia from gene expression analyses. *Molecular Ecology*, 26, 5074–5085. https://doi.org/10.1111/mec.14257

Yuan, W., Liu, S., Zhou, G., Zhou, G., Tieszen, L.L., Baldocchi, D., Bernhofer, C., Gholz, H., Goldstein, A.H., Goulden, M.L., Hollinger, D.Y., Hu, Y., Law, B.E., Stoy, P.C., Vesala, T., Wofsy, S.C., 2007. Deriving a light use efficiency model from eddy covariance flux data for predicting daily gross primary production across biomes. *Agricultural and Forest Meteorology* 143, 189-207. https://doi.org/10.1016/j.agrformet.2006.12.001

Zhao, C., Liu, B., Xiao, L., Hoogenboom, G., Boote, K.J., Kassie, B.T., Pavan, W., Shelia, V., Kim, K.S., Hernandez-Ochoa, I.M., Wallach, D., Porter, C.H., Stockle, C.O., Zhu, Y., Asseng, S., 2019. A simple crop model. *European Journal of Agronomy*, 104, 97–106. https://doi.org/10.1016/j.eja.2019.01.009.

Zianis, D., Mencuccini, M., 2004. On simplifying allometric analyses of forest biomass. *Forest Ecology and Management*, 187, 311–332. https://doi.org/10.1016/j.foreco.2003.07.007

Zwolak, R., Celebias, P., Bogdziewicz, M., 2022. Global patterns in the predator satiation effect of masting: A meta-analysis. *Proceedings of the National Academy of Sciences of the United States of America*, 119. e2105655119 https://doi.org/10.1073/pnas.2105655119

Supplementary Materials

Supplementary Material S1. Full model description

MASTHING (MASting THeory modellING) is a process-based model that simulates mast seeding dynamics by coupling tree structure, phenology, carbon balance, environmental forcing, wood growth and reproductive allocation. The model operates at a daily time step and is driven by meteorological inputs (air temperature, precipitation, incoming radiation) together with tree structural attributes derived from diameter at breast height (DBH). At the core of the framework is a dynamic pool of mobile carbon reserves, hereafter referred to as the resource budget (B_t, g C m^{-2}), which integrates daily carbon gains from photosynthesis and losses due to maintenance respiration and reproductive allocation. All fluxes are expressed per unit crown projection area (CPA, m^2). Reproductive investment is represented as a continuous function of internal resource status and weather cues enabling evaluation of alternative hypotheses about resource-climate coupling.

S1.1. Allometric initialisation

Tree structural properties are initialised from DBH (cm), the only required tree-level input. Crown projection area (CPA, m^2), tree height (H, m) and aboveground biomass components are derived from species-specific allometric relationships (Bartelink, 1997; Zianis & Mencuccini, 2004):

$$CPA = 0.4064 \times DBH^{1.283} \quad \text{SE 1.1}$$

$$H = \exp[1.4192 + 0.5358 \times \ln(DBH)] \quad \text{SE 1.2}$$

$$\ln(B_{tot}) = -1.3816 + 2.3485 \times \ln(DBH) \quad \text{SE 1.3}$$

$$\ln(B_{stem}) = -1.6015 + 2.3427 \times \ln(DBH) \quad \text{SE 1.4}$$

$$\ln(B_{branch}) = -5.2898 + 2.9353 \times \ln(DBH) \quad \text{SE 1.5}$$

$$B_f = 0.0001663 \times DBH^2 \times H + 0.224 \quad \text{SE 1.6}$$

$$LA = 3.38 \times CPA^{1.028} \quad \text{SE 1.7}$$

$$LAI_{max} = (B_f \times SLA) / CPA \quad \text{SE 1.8}$$

where B_{tot} (kg DM) is total aboveground biomass, B_{stem} and B_{branch} (kg DM) are stem and branch biomass, B_f (kg DM) is foliage biomass, LA (m^2) is total leaf area, LAI_{max} is maximum leaf area index, and SLA (m^2 kg^{-1}) is specific leaf area (Table S1.6).

S1.2. Carbon balance dynamics

Daily carbon dynamics are computed as the balance between gross primary production (GPP, g C m^{-2} d^{-1}) and maintenance respiration. GPP is estimated using a light-use efficiency approach:

$$GPP_t = LUE \times GSR_t \times 0.5 \times f_{int} \times f_T \times f_{stress} \quad \text{SE 1.9}$$

where LUE is light use efficiency (g DM MJ^{-1}), GSR_t is global solar radiation (MJ m^{-2} d^{-1}), 0.5 is the PAR fraction, $f_{int} = 1 - \exp(-0.5 \times LAI)$ is the canopy interception fraction, f_T is a temperature

response function (Yan & Hunt, 1999), and f_{stress}= min(f_{heat}, f_{cold}, f_{water}) is the most limiting abiotic stress factor.

The temperature response function returns zero below a minimum ($T_{min,gro}$, °C) and above a maximum ($T_{max,gro}$, °C) temperature threshold

$f_T = 0$, if $T_{avg} \leq T_{min,gro}$ or $T_{avg} \geq T_{max,gro}$ SE 1.10a

$f_T = [(T_{max,gro} - T_{avg})/(T_{max,gro} - T_{opt,gro})] \times [(T_{avg} - T_{min,gro})/(T_{opt,gro} - T_{min,gro})]^{\alpha}$ otherwise SE 1.10b

where $T_{avg} = (T_{max} + T_{min}) / 2$ is mean daily air temperature (°C), T_{opt}, is the optimum temperature for growth (°C), and the exponent α controls the asymmetry of the response:

$\alpha = (T_{opt} - T_{min,gro}) / (T_{max,gro} - T_{opt})$ SE 1.10c

The function rises from zero at $T_{min,gro}$, reaches a maximum of 1.0 at T_{opt}, and returns to zero at $T_{max,gro}$.

Maintenance respiration is computed separately for woody (stem + branches; $R_{wood,t}$, g C m^{-2} d^{-1}) and foliar ($R_{leaf,t}$, g C m^{-2} d^{-1}) components using a Q_{10} formulation:

$R_{wood,t} = RES_w \times Q_{10}^{(Tavg - 25)/10} \times (B_{stem} + B_{branch}) \times 0.5 \times 0.1 \times 1000 / CPA$ SE 1.11a

$R_{leaf,t} = RES_l \times Q_{10}^{(Tavg - 25)/10} \times B_{foliage} \times 0.45 \times (LAI / LAI_{max}) \times 1000 / CPA$ SE 1.11b

where RES_w and RES_l are base respiration rates for wood and leaves respectively (g C g^{-1} DM d^{-1}), and T_{avg} is mean daily air temperature (°C). The factor 0.5 accounts for the carbon content of dry biomass.

Heat stress reduces photosynthesis when daily maximum temperature (T_{max}, °C) exceeds the growth maximum temperature ($T_{max,gro}$, °C). The response is a logistic sigmoid transitioning to zero at the critical heat temperature (T_{heat}, °C):

$m_{heat} = (T_{max,gro} + T_{heat}) / 2$ SE 1.12a

$w_{heat} = T_{heat} - T_{max,gro}$ SE 1.12b

$f_{heat} = 1 / \{1 + \exp[10/ w_{heat} \times (T_{max} - m_{heat})]\}$ SE 1.12c

where $f_{heat} = 1$ when $T_{max} < T_{max,gro}$ (no stress) and $f_{heat} \rightarrow 0$ as T_{max} approaches T_{heat}.

Cold stress reduces photosynthesis when daily minimum temperature (T_{min}, °C) falls below the growth minimum temperature ($T_{min,gro}$, °C). The transition occurs between the critical cold temperature (T_{cold}, °C) and $T_{min,gro}$:

$m_{cold} = (T_{min,gro} + T_{cold}) / 2$ SE 1.13a

$w_{cold} = T_{min,gro} - T_{cold}$ SE 1.13b

$f_{cold} = 1 / \{1 + \exp[10 / (-w_{cold}) \times (T_{min} - m_{cold})]\}$ SE 1.13c

where $f_{cold} = 1$ when $T_{min} > T_{min,gro}$ and f_cold = 0 when $T_{min} \leq T_{cold}$.

Reference evapotranspiration (ET_0, mm d^{-1}) is computed using the Hargreaves method:

$ET_0 = (1/\lambda) \times 0.0023 \times [(T_{max} + T_{min})/2 + 17.8] \times (T_{max} - T_{min})^{0.5} \times R_a$ SE 1.14

where λ $(2.501 - 0.002361 \times T_{avg})$ is the latent heat of vaporization (MJ kg^{-1}), and R_a is extraterrestrial radiation (MJ m^{-2} d^{-1}) computed from site latitude and day of year. A water availability index is then derived from the cumulative balance of ET_0 and precipitation (P, mm) over a moving window of 20 days (WS_{days}):

$$I = (\sum ET_0 - \sum P) / (\sum ET_0 + \sum P + \varepsilon) \quad \text{SE 1.15a}$$

$$W_{avail} = 1 - (I + 1) / 2 \quad \text{SE 1.15b}$$

where $\varepsilon = 10^{-6}$ is a small constant for numerical stability, $I \in [-1, +1]$, and $W_{avail} \in [0, 1]$ (0 = maximum drought, 1 = no stress). The water stress multiplier for GPP is then:

$$f_{water} = 0.5 \times (W_{avail} - WS_{thr}) + 1, \quad \text{if } W_{avail} < WS_{thr} \quad \text{SE 1.15c}$$

$$f_{water} = 1, \quad \text{if } W_{avail} \geq WS_{thr} \quad \text{SE 1.15d}$$

where WS_{thr} is the water stress threshold parameter.

The resource budget evolves daily as a function of phenological stage. Outside the growing season (PhenoCode < 3), only maintenance respiration is active:

$$B_t = \max(0, B_{t-1} - R_{tree,t}) \quad \text{SE 1.16a}$$

During the growing season (PhenoCode 3–5; see Section S1.3), GPP is active and a fraction of daily net carbon gain is directed to wood growth

$$B_t = \max(0, B_{t-1} + (GPP_t - R_{tree,t}) \times (1\text{-}ALL_w \times \delta_{wood,t}) \quad \text{SE 1.16b}$$

where B_t (g C m^{-2}) is the resource budget at day t, $R_{tree,t} = R_{wood,t} + R_{leaf,t}$ is total maintenance respiration, ALL_w is the annual wood allocation coefficient, and $\delta_{wood,t}$ is a phase-dependent modulation factor:

$$\delta_{wood,t} = 1 - f_{rip,t}, \quad \text{if } 3 \leq \text{PhenoCode} \leq 4 \quad \text{SE 1.16c}$$

$$\delta_{wood,t} = 0 \quad \text{if PhenoCode} = 5 \quad \text{SE 1.16d}$$

where $f_{rip,t}$ is the ripening allocation coefficient (SE 1.27). As ripening progresses ($f_{rip,t} \rightarrow 1$), $\delta_{wood,t} \rightarrow 0$ so that carbon is progressively redirected from wood growth to seed filling; during the decline phase (PhenoCode = 5), wood allocation ceases entirely. Additionally, the budget is reduced by daily reproductive investment during the flowering window (Section S1.4) and the greendown phase (Section S1.4).

The maximum resource budget (B_{max}, g C m^{-2}) is set as a fixed fraction of total aboveground biomass:

$$B_{max} = RBF \times B_{tot} \quad \text{SE 1.17}$$

where RBF is the resource budget fraction (calibrated; Table S1.6), controlling the size of the mobile carbon pool relative to structural biomass. The minimum budget required to initiate reproduction (B_{min}, g C m^{-2}) is defined as a threshold fraction of B_{max}:

$$B_{min} = REP_{thr} \times B_{max} \quad \text{SE 1.18}$$

where REP_{thr} is the reproduction threshold (calibrated). The budget is initialised at half the maximum:

$B_0 = B_{max} \times 0.5$ SE 1.19

At the end of each growing season (31 December), the budget is normalised to a dimensionless budget level (BL) serving as the internal state variable for reproductive allocation (Section S1.4):

$BL_t = (B_t - B_{min}) / (B_{max} - B_{min}), \quad BL_t \in [0, 1]$ SE 1.20

S1.3 Phenological development

Tree phenology is simulated using the process-based SWELL model, which tracks dormancy induction, endodormancy, ecodormancy, growth, greendown, and senescence phases through photothermal accumulation. Phenological progression controls the seasonal window of carbon acquisition and the timing of reproductive decisions. A full description is provided in Bajocco et al. (2025). The growing season (PhenoCode 3–5) determines the period over which GPP_t is computed and LAI scales with canopy development. During leaf expansion (growth phase, PhenoCode = 3), LAI increases linearly with growth completion:

$LAI_t = LAI_{max} \times GP_t / 100$ SE 1.21a

During greendown and senescence (phenoCode 4–5), LAI declines in proportion to the normalised vegetation index.

$LAI_t = LAI_{max} \times NDVI_t / NDVI_{max}$ SE 1.21b

where GP_t is the growth completion percentage (%), NDVI is the current vegetation index, and $NDVI_{max}$ is its maximum value at the site (calibrated). The onset of flowering is triggered when growth completion reaches the parameter FLO_t (expressed as a percentage of the full growth forcing requirement).

S1.4 Reproductive allocation

Annual reproductive investment is determined by the combined effects of internal resource status and post-solstice temperature cues. Temperature cues are derived from the inter-annual anomaly of daily maximum temperature over the post-solstice sensing window (DOY 172–212). The anomaly $\Delta T = T_{Y-1} - T_{Y-2}$ (where T_{Y-1} and T_{Y-2} are the mean post-solstice temperatures of the year immediately preceding seed production and the year before it, respectively) encodes both the promoting effect of a warm recent summer and the dampening effect of a warm two-years-prior summer in a single continuous variable. The weather cue WC is computed from ΔT via a Gompertz response function:

$WC_t = A \times \exp\{-\exp[-CUE_s \times (\Delta T_y - \mu)]\}$ SE 1.22

where CUE_s is a sensitivity parameter governing the steepness of the response, $\mu = (\Delta T_{min} + \Delta T_{max}) / 2$ is the midpoint of the site-specific range of inter-annual temperature anomalies, and A is the asymptote (A = 1 in RB+WC; $A = BL_t$ in RB×WC). The site-specific scaling parameters ΔT_{min} and

ΔT_{max} span the range of observed inter-annual temperature anomalies at each site and are derived from the historical meteorological record as follows:

$\Delta T_y = \text{mean}(T_{max,d}, d \in [172, 212], Y-1) - \text{mean}(T_{max,d}, d \in [172, 212], Y-2)$ SE 1.23a

$\Delta T_{min} = \min(\Delta T_y)$ over all years in record SE1.23b

$\Delta T_{max} = \max(\Delta T_y)$ over all years in record SE1.23c

This data-driven scaling ensures that the Gompertz response spans the full range of ΔT variability observed at each site, so the normalised cue signal reflects relative rather than absolute temperature anomalies. In the RB+WC formulation A = 1, so $WC_t \in [0, 1]$ independently of the resource state; in RB×WC, A = BL_t, so the cue is bounded by the current budget level, producing a resource-gated response in which a favourable temperature signal can only promote reproduction in proportion to accumulated reserves. In both weather-cue variants the output is clipped to [0, 1].

Reproductive potential (RP) emerges as a continuous function of resource availability and climatic forcing, with the cue weight CUE_W fixed at 0.49 in all experiments presented here:

$RP_t = BL_t$ (RB formulation) SE 1.24a

$RP_t = (1\text{-}CUE_w) \times BL_t + (CUE_w \times WC_t)$ (RB+WC, RB×WC formulations) SE 1.24b

Reproductive investment (I_{rep}, g C m^{-2}) is computed as the minimum of available reserves and potential investment, and partitioned between flowering and fruit development:

$I_{rep} = \min(B_t, RP_t \times B_{max})$ SE 1.25a

$I_{seed} = I_{rep} / (1 + FFC)$ SE 1.25b

$I_{flow} = I_{rep} - I_{seed}$ SE 1.25c

where FCC is the flowers-to-fruit cost, the additional carbon cost of flower production relative to seed ripening. Realised reproduction is further reduced by unfavourable conditions during flowering and seed development. Pollination efficiency is computed as a sigmoidal function of daily precipitation during the flowering window ($Flo_t \pm Flo_d$ /2):

$f_{poll} = 1 / \{1 + \exp[k \times (P_{day} - P_{mid})]\}$ SE 1.26a

where the sensitivity parameter k and the midpoint P_{mid} are derived from the precipitation threshold POL_p

$k = POL_p \times (1 - POL_p / 50)$ SE 1.26b

$P_{mid} = POL_p / 2$ SE 1.26c

High precipitation during anthesis reduces pollination efficiency, scaling down flowering and ripening investment proportionally. During the greendown phase, seed ripening progresses following a logistic function of greendown completion (GD%, %), modulated by water stress:

$f_{rip} = 1 / \{1 + \exp[-k_r \times (GD\% - 50)]\}$ SE 1.27

where $k_r = 0.09$ is a fixed parameter controlling the steepness of the ripening response.

Resources saved by incomplete ripening under drought stress are returned to the budget. Budget deductions for reproductive investment occur daily throughout the active reproductive window: flowering investment is deducted during the pollination window in proportion to the daily change in pollination potential; ripening investment is deducted daily during the greendown phase in proportion to the daily ripening rate. The budget available at the start of the following year therefore reflects the cumulative effect of all daily deductions:

$$B_{t+1,init} = B_t - I_{rep} + R_{veto} \quad \text{SE 1.28}$$

where R_{veto} (g C m^{-2} d^{-1}) represents resources recovered from incomplete seed ripening. This carry-over links past reproductive investment to future carbon availability, generating the interannual feedbacks characteristic of masting systems.

S1.5 Wood growth

Net carbon not allocated to reproduction is partitioned to wood growth following a dynamic scheme. The annual carbon available for wood growth ($C_{wood,t}$, g C m^{-2}) is computed as the fraction of daily net carbon gain directed to structural growth, integrated over the growing season. The wood allocation coefficient is set annually and depends on the reproductive potential of the prior year:

$$f_{wood,t} = ALL_w \times (1 - RP_{t-1}) \quad \text{SE 1.29}$$

where $f_{wood,max}$ is the maximum wood allocation fraction, and RP_{t-1} is the reproductive potential of the preceding year (see SE1.24b). This formulation ensures that years following high reproductive expenditure direct proportionally less carbon to structural growth, coupling reproductive and growth dynamics. Note that $f_{wood,t}$ is further modulated daily by $\delta_{wood,t}$ (SE1.16c–d), which progressively redirects carbon from wood to seed filling as ripening advances.

Annual ring width increment (ΔRW_t, mm yr^{-1}) is then derived from $C_{wood,t}$ through an allometric conversion:

$$\Delta RW_t = RNG_w \times C_{wood,t} \times f_{water,t} \quad \text{SE 1.30a}$$

where RNG_w is the ring width conversion factor (mm g^{-1} m^{-2}) and $f_{water,t}$ is the water stress factor (SE1.15c–d). DBH is updated cumulatively:

$$DBH_{t+1} = DBH_t + (2 \times \Delta RW_t) / 10 \quad \text{SE 1.30b}$$

S1.6 Model formulations

Three alternative formulations of reproductive allocation were evaluated. In the RB formulation, reproduction depends exclusively on internal reserves ($RP_t = BL_t$; SE 1.24a), and temperature cues do not enter the allocation rule. In the RB+WC formulation, cues contribute additively to reproductive potential (SE 1.24b) but act independently of resource status (A = 1 in SE 1.22), so warm post-solstice

temperatures promote reproduction regardless of current reserves. In the RB×WC formulation, cue sensitivity is explicitly modulated by the normalised budget level ($A = BL_t$ in SE1.22), so favourable cues amplify reproduction only when reserves are sufficient. These three formulations represent alternative hypotheses about resource–climate coupling and are compared against the same observational dataset.

Supplementary Material S2. Resource-modulated temperature cue function

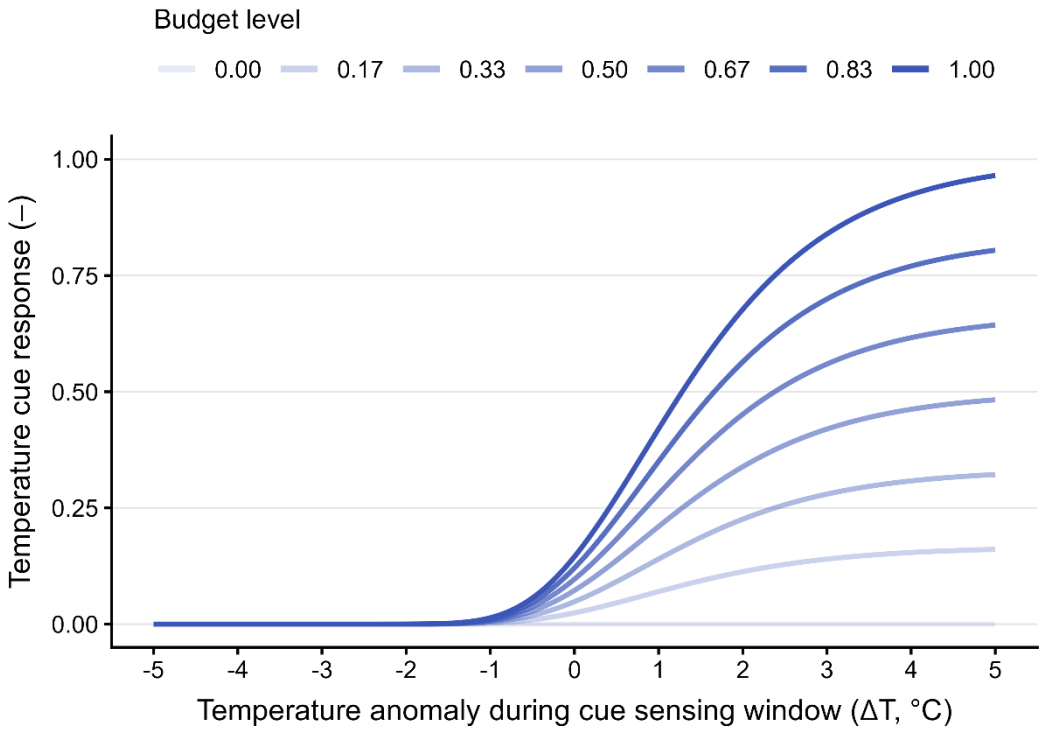

Figure S2. Resource-modulated Gompertz weather cue function governing reproductive investment in the RB×WC model formulation. Curves show the theoretical relationship between the inter-annual temperature anomaly ($\Delta T = T_{Y-1} - T_{Y-2}$, °C) computed over the post-solstice sensing window (DOY 172–212) and the dimensionless weather cue response $WC_t \in [0, 1]$, computed via the Gompertz function (Equation 1 in the main text) with asymptote A set equal to the normalised resource budget level (BLt). Each curve corresponds to a different budget level ($A = BL_t$, ranging from 0.00 to 1.00 in equal steps); line transparency decreases as resource availability declines. Because $A = BL_t$, the budget level sets the ceiling of the cue response: even a strong temperature signal cannot drive WC_t above the current level of carbon reserves, producing the resource-gated behaviour characteristic of the RB×WC formulation (see the main tet). The sensitivity parameter k and midpoint μ are held at their calibrated values for illustration.

Supplementary Material S3. Study sites overview

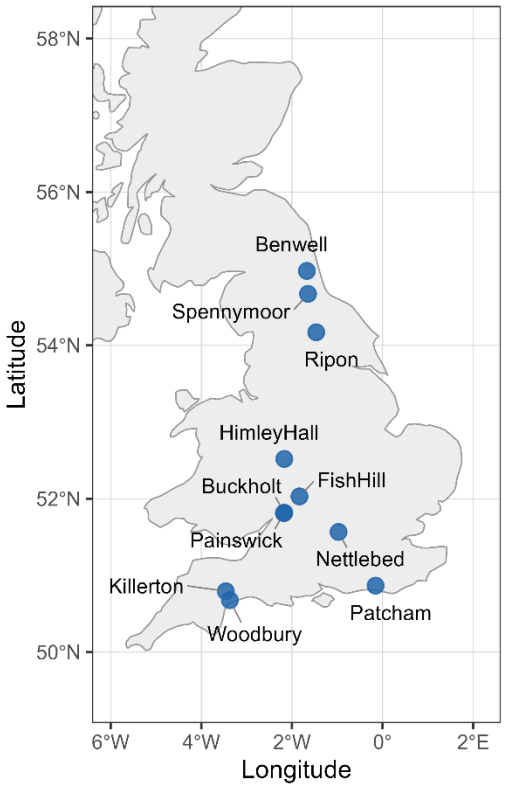

Site	N trees	First yr	Last yr	N obs
Benwell	10	1983	2025	314
Spennymoor	10	1981	2024	317
Ripon	12	1981	2024	392
HimleyHall	5	1981	2025	174
FishHill	10	2007	2025	190
Buckholt	8	1982	2025	331
Painswick	5	1980	2025	162
Nettlebed	12	1981	2025	286
Patcham	9	1980	2025	236
Killerton	6	1980	2025	183
Woodbury	10	1980	2025	340

Figure S3. Geographic distribution and characteristics of the 11 UK beech study sites. Left panel: site locations across England. Right panel: site-level summary statistics including number of monitored trees (after excluding trees with fewer than 10 years of observations), observation period, and total number of seed production records

Supplementary Material S4. Results of the sensitivity analysis for all parameters

Table S4. Morris OAT global sensitivity analysis results for all 23 parameters. Values are means and standard deviation (SD) of main absolute elementary effect (μ*) and standard deviation of elementary effects (σ) across the eleven study sites and three model formulations (RB, RB+WC, RB×WC). C_{seed} units: gC m^{-2}; CV_{seed} is dimensionless. Parameters acronyms are explained in Table 1 of the main text and are ordered by decreasing max(μ* C_{seed}, μ* CV_{seed}).

Parameter	C_{seed}				CV_{seed}			
	μ*	μ* SD	σ	σ SD	μ*	μ* SD	σ	σ SD
LUE	483.55	41.19	61.41	7.78	0.12	0.06	0.37	0.28
DBH	276.27	23.15	109.33	6.17	0.17	0.08	0.52	0.30
Q_{10}	245.66	12.72	95.82	5.83	0.12	0.09	0.36	0.27
RES_l	237.63	9.44	80.67	2.92	0.10	0.07	0.33	0.29
ECO	78.30	8.81	37.24	9.63	0.14	0.07	0.33	0.27
RES_w	75.46	4.46	29.87	1.40	0.08	0.05	0.37	0.23
FFC	60.72	8.50	30.12	2.73	0.02	0.02	0.04	0.03
SLA	54.69	4.27	36.01	2.86	0.03	0.03	0.16	0.21
ALL_w	49.29	7.00	15.54	1.86	0.03	0.02	0.07	0.07
WS_{thr}	45.84	6.14	13.41	1.49	0.05	0.03	0.22	0.22

GRO	38.17	5.56	19.34	8.09	0.10	0.06	0.33	0.29
POL_p	24.07	6.68	24.23	8.21	0.15	0.05	0.23	0.20
RBF	20.69	8.92	19.89	4.13	0.06	0.04	0.20	0.26
FLO_d	19.52	6.39	29.98	13.56	0.15	0.07	0.33	0.26
FLO_t	19.38	8.51	33.89	17.04	0.14	0.05	0.26	0.16
GRD	19.12	4.50	8.49	1.56	0.04	0.03	0.20	0.18
RNG_w	15.48	2.55	11.23	2.15	0.05	0.06	0.30	0.37
REP_{thr}	9.85	4.67	13.75	4.32	0.28	0.23	0.25	0.26
CUE_w	9.32	11.54	7.17	7.33	0.06	0.07	0.04	0.03
CUE_s	2.10	1.94	2.83	2.68	0.04	0.04	0.04	0.11
T_{cold}	2.03	0.85	1.57	1.22	0.01	0.02	0.08	0.23
SEN	1.74	0.77	2.65	2.21	0.02	0.03	0.12	0.27
T_{heat}	0.05	0.07	0.03	0.05	0.00	0.00	0.00	0.00

Supplementary Material S5. Site-level model performance under site-specific and domain-wide parameterisation

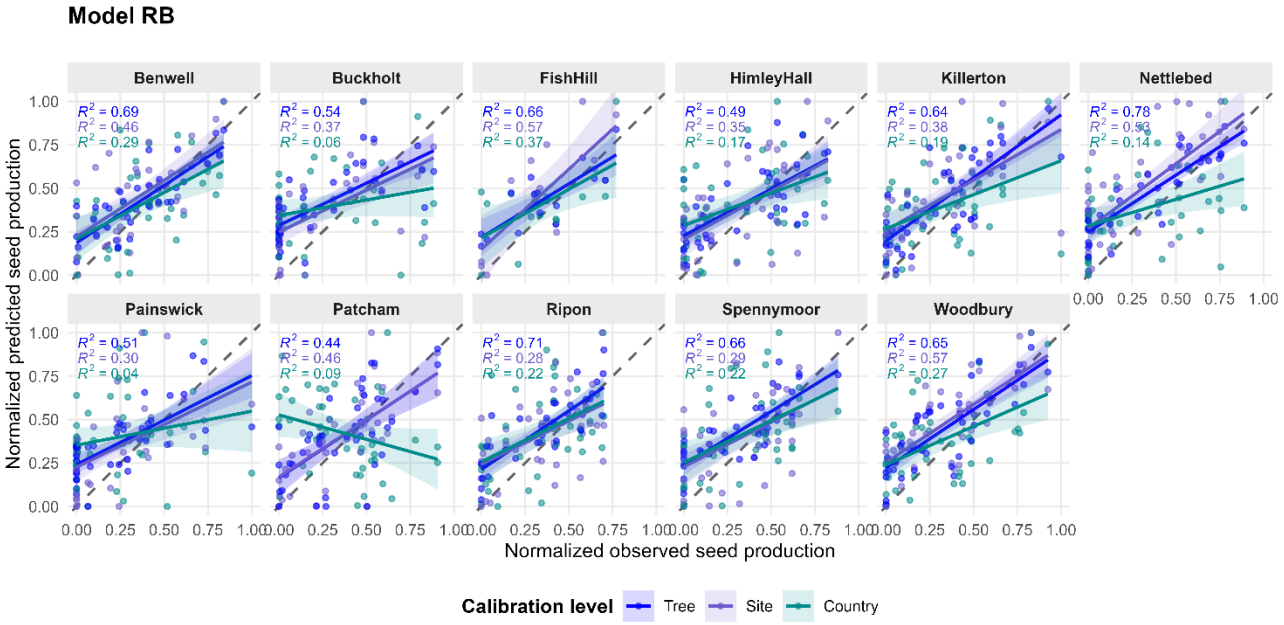

Figure S5.1. Site-level model performance across calibration scales for the RB formulation. Each panel shows the relationship between observed and simulated normalised seed production at a single site, with separate regression lines for tree-level (dark blue), site-level (purple), and country-wide (green) calibration. R^2 values are reported for each calibration level. The dashed 1:1 line denotes perfect agreement. Tree-level calibration optimises parameters independently for each individual tree; site-level calibration uses a single parameter set estimated from all trees within a site; country-wide calibration uses a single parameter set estimated jointly across all sites.

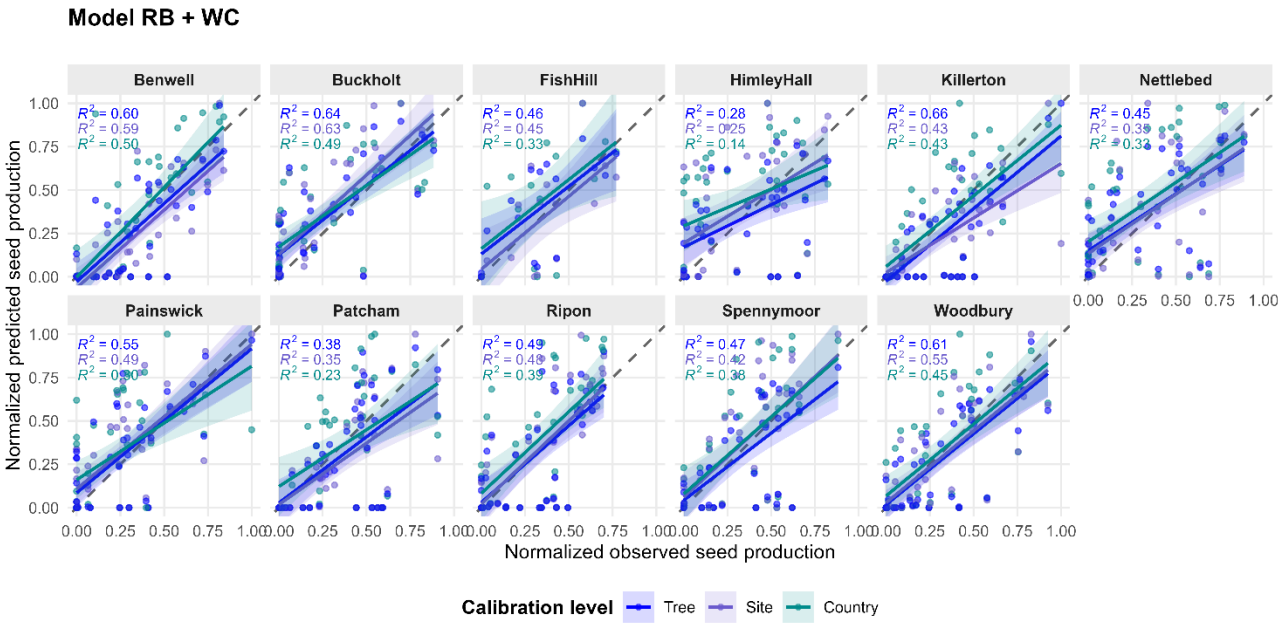

Figure S5.2. Site-level model performance across calibration scales for the **RB+WC** formulation. Each panel shows the relationship between observed and simulated normalised seed production at a single site, with separate regression lines for tree-level (dark blue), site-level (purple), and country-wide (green) calibration. R^2 values are reported for each calibration level. The dashed 1:1 line denotes perfect agreement. See Figure S5.1 for a description of calibration levels.

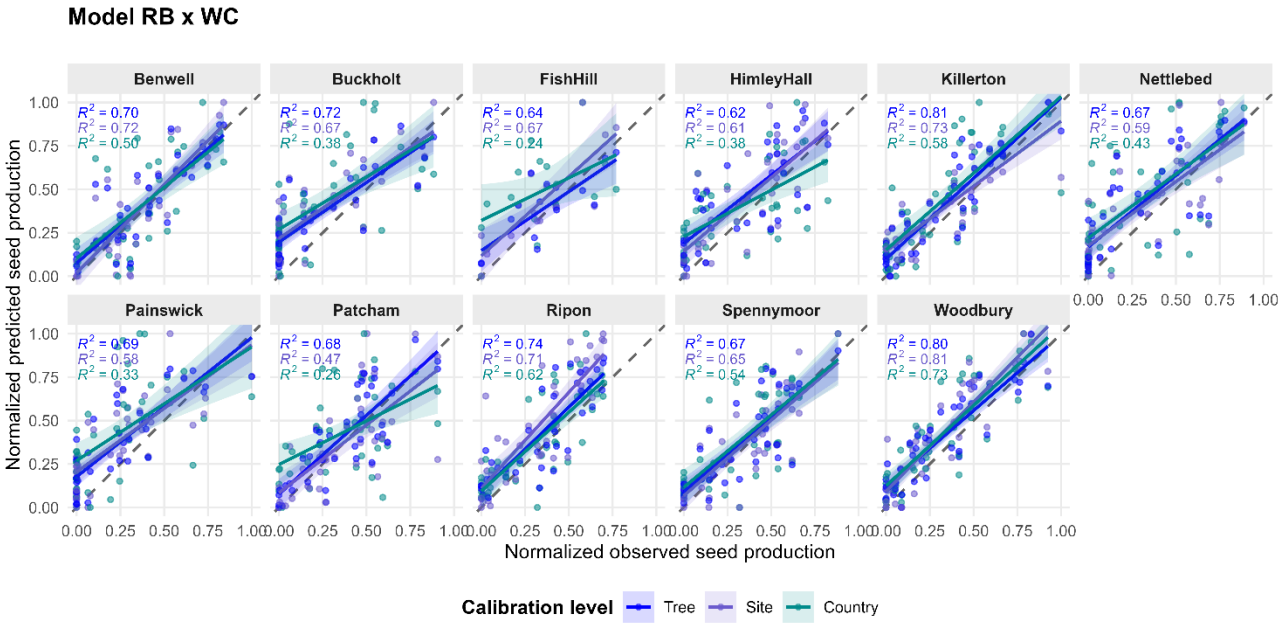

Figure S5.3. Site-level model performance across calibration scales for the **RB×WC** formulation. Each panel shows the relationship between observed and simulated normalised seed production at a single site, with separate regression lines for tree-level (dark blue), site-level (purple), and country-wide (green) calibration. R^2 values are reported for each calibration level. The dashed 1:1 line denotes perfect agreement. See Figure S5.1 for a description of calibration levels.

Supplementary Material S6. Calibrated parameter values across model versions and spatial scales

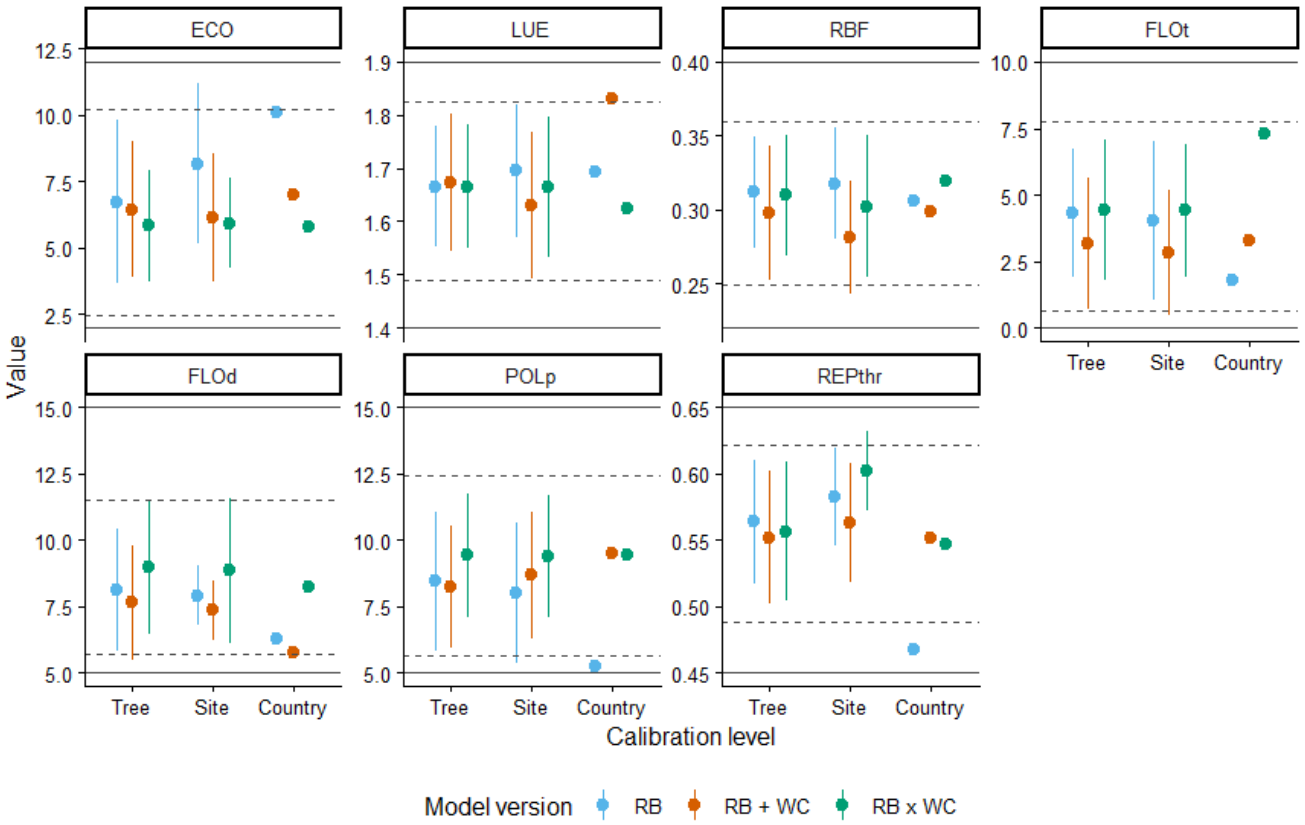

Figure S6.1. Calibrated values (mean ± 1 SD) of the seven MASTHING parameters — ecodormancy photothermal threshold (ECO), light-use efficiency (LUE), resource budget fraction (RBF), flowering time (FLOt), flowering duration (FLOd), limiting pollination precipitation (POLp), and reproduction threshold (REPthr) — shown for each model version (RB, RB+WC, RB×WC) across the three calibration levels: individual trees (Tree), site-level aggregate (Site), and country-pooled fit (Country). Solid horizontal lines mark the parameter bounds used during optimisation; dashed lines indicate the 10th and 90th percentiles of the tree-level calibrated distribution across all sites.

Table S6.2. Calibrated values of the seven MASTHING parameters for each site, calibration level (Tree: individual-tree calibration, mean ± SD over *n* trees; Site: single site-level calibration; Country: single national-level calibration), and model version (RB, RB+WC, RB×WC). Parameter acronyms as in Table 1 of the main text and caption of Figure S6.1.

Site	Calib. level	Model version	Parameter						
			ECO	LUE	RBF	FLOt	FLOd	POLp	REPthr
Benwell	Tree	RB	6.7 ± 2.5	1.71 ± 0.11	0.33 ± 0.03	4.1 ± 2.8	7.4 ± 1.8	8.5 ± 3.6	0.57 ± 0.06
		RB + WC	6.3 ± 1.2	1.66 ± 0.12	0.31 ± 0.03	2.0 ± 1.1	7.0 ± 1.2	7.6 ± 1.9	0.54 ± 0.04
		RB x WC	5.3 ± 1.4	1.64 ± 0.12	0.30 ± 0.05	4.9 ± 2.4	7.5 ± 2.4	8.9 ± 2.1	0.57 ± 0.05
	Site	RB	3.4	1.77	0.29	3.2	6.8	10.2	0.63

		RB + WC	6.8	1.59	0.24	0.5	7.3	7.6	0.57
		RB x WC	5.3	1.63	0.38	4.5	9.8	8.2	0.62
Buckholt	Tree	RB	9.3 ± 2.9	1.62 ± 0.15	0.32 ± 0.03	3.3 ± 2.0	8.0 ± 1.9	6.4 ± 1.6	0.56 ± 0.05
		RB + WC	5.9 ± 1.3	1.61 ± 0.10	0.31 ± 0.03	4.6 ± 2.7	8.4 ± 2.3	8.4 ± 2.1	0.56 ± 0.07
		RB x WC	6.3 ± 2.6	1.58 ± 0.09	0.28 ± 0.03	5.9 ± 3.2	9.5 ± 2.5	9.6 ± 2.7	0.52 ± 0.06
	Site	RB	10.8	1.75	0.3	1	8.1	5.3	0.65
		RB + WC	7.2	1.78	0.3	2.6	8.4	10.6	0.52
		RB x WC	7	1.66	0.3	7.8	8.1	12.2	0.54
FishHill	Tree	RB	9.7 ± 1.6	1.69 ± 0.16	0.30 ± 0.03	5.6 ± 2.4	7.8 ± 2.6	6.8 ± 1.4	0.58 ± 0.06
		RB + WC	6.8 ± 3.8	1.77 ± 0.12	0.27 ± 0.05	3.3 ± 3.4	6.6 ± 2.0	7.8 ± 2.4	0.54 ± 0.04
		RB x WC	7.7 ± 2.1	1.64 ± 0.11	0.33 ± 0.03	4.5 ± 3.4	6.8 ± 1.4	9.9 ± 3.1	0.51 ± 0.04
	Site	RB	9.7	1.56	0.29	8.7	7.9	6.8	0.6
		RB + WC	3.3	1.43	0.23	2.1	5.4	6.9	0.47
		RB x WC	6.9	1.46	0.31	6.3	5.1	9.3	0.61
HimleyHall	Tree	RB	9.3 ± 0.9	1.69 ± 0.12	0.28 ± 0.04	4.7 ± 3.3	9.3 ± 2.2	6.3 ± 0.6	0.55 ± 0.04
		RB + WC	8.0 ± 2.0	1.69 ± 0.10	0.27 ± 0.04	5.1 ± 2.2	8.9 ± 3.2	5.7 ± 0.7	0.59 ± 0.06
		RB x WC	5.6 ± 1.3	1.73 ± 0.14	0.29 ± 0.02	5.8 ± 1.5	9.5 ± 2.8	7.9 ± 1.8	0.58 ± 0.05
	Site	RB	9.5	1.66	0.29	1.2	7.8	6.4	0.59
		RB + WC	10	1.48	0.35	0.2	7.7	6	0.63
		RB x WC	6.3	1.72	0.29	0.3	11.8	8.2	0.62
Killerton	Tree	RB	7.9 ± 3.0	1.65 ± 0.06	0.34 ± 0.02	3.9 ± 2.2	8.4 ± 3.3	7.3 ± 0.9	0.54 ± 0.04
		RB + WC	8.4 ± 1.2	1.63 ± 0.11	0.32 ± 0.05	2.9 ± 1.4	6.2 ± 0.8	7.9 ± 1.6	0.57 ± 0.05
		RB x WC	6.7 ± 0.6	1.70 ± 0.12	0.32 ± 0.03	3.5 ± 1.7	10.6 ± 2.5	11.0 ± 1.6	0.57 ± 0.05
	Site	RB	10.4	1.87	0.34	2.2	9.9	5.7	0.53
		RB + WC	7.5	1.63	0.32	5.4	6.4	9.2	0.6
		RB x WC	6	1.71	0.33	4	8.8	7.9	0.55
Nettlebed	Tree	RB	3.8 ± 1.5	1.66 ± 0.13	0.30 ± 0.04	3.6 ± 1.9	8.0 ± 2.5	10.3 ± 2.6	0.57 ± 0.05
		RB + WC	5.4 ± 2.8	1.68 ± 0.12	0.28 ± 0.03	2.5 ± 2.7	8.2 ± 2.7	7.1 ± 1.2	0.56 ± 0.05
		RB x WC	4.2 ± 2.2	1.61 ± 0.11	0.29 ± 0.04	4.4 ± 2.8	9.8 ± 2.9	9.3 ± 2.0	0.57 ± 0.06
	Site	RB	7.5	1.63	0.36	5.7	8.3	11.2	0.58
		RB + WC	2.6	1.57	0.31	1.5	6.3	7.1	0.59
		RB x WC	2.1	1.63	0.24	5.6	6.9	8.7	0.64
Painswick	Tree	RB	3.4 ± 1.7	1.73 ± 0.11	0.31 ± 0.04	2.3 ± 1.3	8.3 ± 1.6	9.3 ± 2.5	0.56 ± 0.04
		RB + WC	5.3 ± 1.7	1.69 ± 0.05	0.27 ± 0.03	5.1 ± 1.8	9.0 ± 0.6	8.3 ± 2.1	0.58 ± 0.05
		RB x WC	5.5 ± 2.1	1.71 ± 0.09	0.29 ± 0.03	6.8 ± 2.0	8.6 ± 3.0	10.3 ± 3.5	0.55 ± 0.05
	Site	RB	11.7	1.84	0.34	2.8	6.6	7	0.6
		RB + WC	6.6	1.68	0.26	8.1	6.3	11.7	0.53
		RB x WC	7.1	1.87	0.39	8	8	11.7	0.61
Patcham	Tree	RB	2.7 ± 0.5	1.64 ± 0.10	0.31 ± 0.03	5.2 ± 3.2	7.8 ± 1.4	10.6 ± 2.7	0.59 ± 0.02
		RB + WC	2.7 ± 0.8	1.64 ± 0.15	0.33 ± 0.04	3.0 ± 1.2	8.6 ± 2.7	7.6 ± 1.7	0.57 ± 0.05
		RB x WC	4.5 ± 2.4	1.73 ± 0.12	0.30 ± 0.04	3.2 ± 2.9	9.3 ± 3.5	10.4 ± 2.5	0.56 ± 0.06
	Site	RB	2.5	1.6	0.39	8.1	8.6	12.6	0.57
		RB + WC	2.3	1.45	0.26	1	8.9	6.1	0.56
		RB x WC	4.4	1.49	0.26	1.7	8.6	7.5	0.59
Ripon	Tree	RB	6.6 ± 2.1	1.65 ± 0.11	0.31 ± 0.05	5.2 ± 2.5	7.4 ± 2.4	9.1 ± 3.0	0.55 ± 0.06

		RB + WC	7.3 ± 1.4	1.69 ± 0.14	0.30 ± 0.05	3.0 ± 2.7	7.2 ± 1.2	9.9 ± 2.9	0.54 ± 0.05
		RB x WC	6.8 ± 1.9	1.66 ± 0.15	0.32 ± 0.04	2.9 ± 1.5	8.4 ± 1.5	9.3 ± 2.2	0.54 ± 0.04
	Site	RB	7.3	1.46	0.26	7.6	6.5	5	0.53
		RB + WC	7.8	1.79	0.26	2.1	8	13.3	0.59
		RB x WC	8.2	1.55	0.29	1.9	5.9	13.5	0.62
Spennymoor	Tree	RB	5.6 ± 1.9	1.64 ± 0.10	0.30 ± 0.03	4.2 ± 2.6	8.2 ± 2.4	8.3 ± 2.3	0.57 ± 0.04
		RB + WC	7.8 ± 1.7	1.65 ± 0.17	0.33 ± 0.05	1.8 ± 2.6	6.5 ± 1.3	10.6 ± 2.4	0.54 ± 0.04
		RB x WC	5.8 ± 1.5	1.69 ± 0.08	0.34 ± 0.03	4.1 ± 3.3	8.8 ± 1.7	8.7 ± 2.2	0.57 ± 0.05
	Site	RB	6.9	1.8	0.3	0.5	7.1	10.5	0.57
		RB + WC	6.7	1.75	0.3	4.1	7.8	7.6	0.53
		RB x WC	7	1.74	0.29	2.9	9.6	6	0.61
Woodbury	Tree	RB	9.7 ± 1.2	1.67 ± 0.08	0.33 ± 0.04	4.0 ± 1.4	9.7 ± 2.7	8.2 ± 1.7	0.56 ± 0.04
		RB + WC	7.6 ± 2.7	1.66 ± 0.14	0.27 ± 0.05	3.6 ± 2.5	8.5 ± 2.5	8.0 ± 1.8	0.53 ± 0.04
		RB x WC	5.8 ± 1.5	1.69 ± 0.10	0.33 ± 0.05	4.9 ± 1.6	10.6 ± 1.9	8.9 ± 1.7	0.59 ± 0.03
	Site	RB	10.3	1.69	0.34	3.4	9.4	7.4	0.56
		RB + WC	6.9	1.78	0.26	3.6	8.3	9.4	0.59
		RB x WC	4.9	1.85	0.25	5.5	14.9	10.4	0.62
All sites	Country	RB	10.1	1.69	0.31	1.8	6.3	5.2	0.47
		RB + WC	7	1.83	0.3	3.3	5.8	9.5	0.55
		RB x WC	5.8	1.62	0.32	7.3	8.2	9.4	0.55

Table S6.3. Parameters held constant across all model formulations and sites, either constrained by literature ranges or set to species-representative values (see Table S6.2 for calibrated parameters).

Symbol	Description	Value
T_{heat}	Critical heat temperature (°C)	36
T_{cold}	Critical cold temperature (°C)	0
WS_{thr}	Water stress threshold (–)	0.55
RES_w	Relative wood respiration (day^{-1})	0.0002
RES_l	Relative leaf respiration (day^{-1})	0.029
Q_{10}	Temperature sensitivity of respiration (–)	2
SLA	Specific leaf area ($m^2\ kg^{-1}$)	21
ALL_w	Wood allocation fraction maximum (–)	0.44
RNG_w	Ring width conversion factor ($mm\ g^{-1}\ m^{-2}$)	0.004
FFC	Flower-to-fruit cost (–)	0.23
CUE_s	Temperature cue sensitivity (–)	2
CUE_w	Temperature cue weight (–)	0.49

Supplementary Material S7. Per-class model classification performance

Table S7.1. Per-class classification performance of the three model versions across the three calibration levels. Each row corresponds to one of the four seed production categories: Failure [0, 0.25), Low [0.25, 0.50), High [0.50, 0.75), Mast [0.75, 1], within a given model–calibration combination. Metrics are computed using a one-vs-rest approach: for each class, all other classes are pooled as "negative", and true positives (TP), false negatives (FN), false positives (FP), and true

negatives (TN) are derived from the corresponding row and column of the confusion matrix. *N* is the number of test observations belonging to that class (TP + FN). POD (Probability of Detection) = TP / (TP + FN); Specificity = TN / (TN + FP); Precision = TP / (TP + FP); F1 = 2·TP / (2·TP + FP + FN); CSI (Critical Success Index) = TP / (TP + FN + FP). Total test set size: 2,706 tree-year observations.

Model version	Calibration	Class	n_obs	POD	Specificity	Precision	F1	CSI
RB	Country	Failure	1333	0.347	0.862	0.709	0.465	0.303
RB	Country	Low	609	0.516	0.550	0.250	0.336	0.202
RB	Country	High	470	0.238	0.809	0.208	0.222	0.125
RB	Country	Mast	294	0.194	0.917	0.221	0.207	0.115
RB + WC	Country	Failure	1333	0.617	0.739	0.696	0.654	0.486
RB + WC	Country	Low	609	0.159	0.852	0.238	0.191	0.105
RB + WC	Country	High	470	0.345	0.763	0.234	0.279	0.162
RB + WC	Country	Mast	294	0.415	0.874	0.286	0.339	0.204
RB x WC	Country	Failure	1333	0.544	0.851	0.780	0.641	0.471
RB x WC	Country	Low	609	0.299	0.732	0.244	0.269	0.155
RB x WC	Country	High	470	0.370	0.781	0.262	0.307	0.181
RB x WC	Country	Mast	294	0.323	0.887	0.259	0.287	0.168
RB	Site	Failure	1333	0.369	0.907	0.794	0.504	0.337
RB	Site	Low	609	0.412	0.592	0.227	0.293	0.171
RB	Site	High	470	0.353	0.762	0.237	0.284	0.166
RB	Site	Mast	294	0.350	0.927	0.368	0.359	0.219
RB + WC	Site	Failure	1333	0.717	0.698	0.698	0.707	0.547
RB + WC	Site	Low	609	0.233	0.826	0.280	0.254	0.146
RB + WC	Site	High	470	0.291	0.841	0.278	0.285	0.166
RB + WC	Site	Mast	294	0.367	0.905	0.320	0.342	0.207
RB x WC	Site	Failure	1333	0.563	0.917	0.868	0.683	0.518
RB x WC	Site	Low	609	0.453	0.674	0.288	0.352	0.213
RB x WC	Site	High	470	0.349	0.840	0.315	0.331	0.198
RB x WC	Site	Mast	294	0.503	0.912	0.410	0.452	0.292
RB	Tree	Failure	1333	0.471	0.907	0.831	0.601	0.430
RB	Tree	Low	609	0.415	0.672	0.269	0.326	0.195
RB	Tree	High	470	0.419	0.786	0.291	0.344	0.208
RB	Tree	Mast	294	0.510	0.924	0.450	0.478	0.314
RB + WC	Tree	Failure	1333	0.713	0.713	0.707	0.710	0.550
RB + WC	Tree	Low	609	0.310	0.804	0.315	0.313	0.185
RB + WC	Tree	High	470	0.328	0.863	0.334	0.331	0.198
RB + WC	Tree	Mast	294	0.483	0.934	0.472	0.477	0.313
RB x WC	Tree	Failure	1333	0.638	0.897	0.857	0.732	0.577
RB x WC	Tree	Low	609	0.420	0.734	0.315	0.360	0.220
RB x WC	Tree	High	470	0.357	0.828	0.304	0.329	0.197
RB x WC	Tree	Mast	294	0.541	0.922	0.457	0.495	0.329

Supplementary Material S8. Model performance in simulating wood growth and NDVI

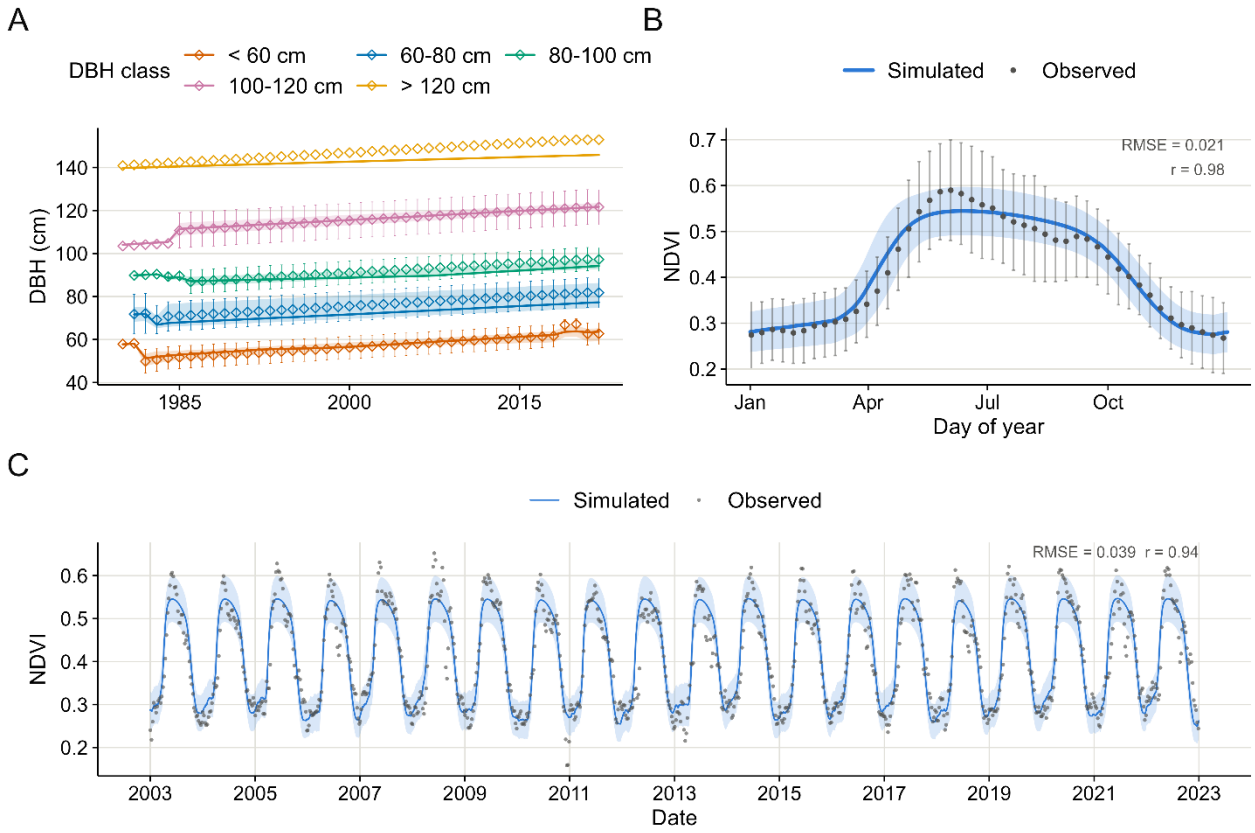

Figure S8.1. Structural and phenological validation of MASTHING. (A) Simulated (lines) and observed (circles ± SD) diameter at breast height (DBH) trajectories for five initial size classes (< 60, 60–80, 80–100, 100–120, and > 120 cm) over the full simulation period (~1980–2020). Size-class rank order is preserved throughout the simulation. (B) Mean seasonal NDVI dynamics averaged across sites and years: simulated values (line) versus MODIS observations (circles); r = 0.98, RMSE = 0.021. (C) Interannual NDVI time series from 2003 to 2023: simulated (line) versus MODIS observations (circles); r = 0.94, RMSE = 0.039. In (B) and (C), shaded bands and error bars represent ± 1 SD across sites.

Supplementary Material S9. Temporal dynamics of reproductive failure across model formulations

Table S9.1 Simulated and observed masting intensity (CV_p) and proportion of reproductive failure years across time windows and calibration levels. CV_p was computed as the coefficient of variation of annual normalised seed production over 10-year moving windows with a 5-year step; values are reported as the final year of each window (Period; e.g., 1990 corresponds to 1980–1990). Reproductive failures were defined as years with normalised seed production < 0.25. CV_p and failure proportions were first computed per site within each window, then averaged across sites. Calibration levels refer to the spatial scale at which model parameters were estimated: all sites pooled (Country), individual sites (Site), and individual trees within sites (Tree). Simulated values (CVp_sim, Fail_sim) are compared against observed values (CVp_obs, Fail_obs), which are independent of calibration level.

Calib. level	Model version	Period	CVp_sim	CVp_obs	Fail_sim	Fail_obs
Country	RB	1990	0.597	1.048	0.285	0.509
	RB	1995	0.431	1.081	0.172	0.537
	RB	2000	0.559	1.053	0.282	0.558
	RB	2005	0.83	1.132	0.452	0.56
	RB	2010	0.576	1.055	0.277	0.553
	RB	2015	0.569	0.955	0.238	0.503
	RB	2020	0.543	0.878	0.19	0.448
	RB	2025	0.393	0.731	0.108	0.362
	RB + WC	1990	0.89	1.048	0.446	0.509
	RB + WC	1995	0.908	1.081	0.456	0.537
	RB + WC	2000	0.976	1.053	0.481	0.558
	RB + WC	2005	1.111	1.132	0.513	0.56
	RB + WC	2010	0.819	1.055	0.363	0.553
	RB + WC	2015	0.762	0.955	0.337	0.503
	RB + WC	2020	0.919	0.878	0.452	0.448
	RB + WC	2025	0.925	0.731	0.449	0.362
	RB x WC	1990	0.748	1.048	0.394	0.509
	RB x WC	1995	0.662	1.081	0.322	0.537
	RB x WC	2000	0.634	1.053	0.34	0.558
	RB x WC	2005	0.782	1.132	0.442	0.56
	RB x WC	2010	0.819	1.055	0.462	0.553
	RB x WC	2015	0.626	0.955	0.306	0.503
	RB x WC	2020	0.506	0.878	0.262	0.448
	RB x WC	2025	0.464	0.731	0.2	0.362
Site	RB	1990	0.606	1.048	0.289	0.509
	RB	1995	0.442	1.081	0.19	0.537
	RB	2000	0.476	1.053	0.196	0.558
	RB	2005	0.655	1.132	0.311	0.56
	RB	2010	0.653	1.055	0.304	0.553
	RB	2015	0.618	0.955	0.251	0.503
	RB	2020	0.532	0.878	0.168	0.448
	RB	2025	0.394	0.731	0.136	0.362
	RB + WC	1990	0.959	1.048	0.49	0.509

	RB + WC	1995	0.974	1.081	0.488	0.537
	RB + WC	2000	1.097	1.053	0.607	0.558
	RB + WC	2005	1.21	1.132	0.61	0.56
	RB + WC	2010	0.892	1.055	0.392	0.553
	RB + WC	2015	0.834	0.955	0.411	0.503
	RB + WC	2020	1.014	0.878	0.545	0.448
	RB + WC	2025	1.028	0.731	0.531	0.362
	RB x WC	1990	0.779	1.048	0.42	0.509
	RB x WC	1995	0.707	1.081	0.385	0.537
	RB x WC	2000	0.66	1.053	0.369	0.558
	RB x WC	2005	0.806	1.132	0.417	0.56
	RB x WC	2010	0.838	1.055	0.434	0.553
	RB x WC	2015	0.639	0.955	0.305	0.503
	RB x WC	2020	0.534	0.878	0.224	0.448
	RB x WC	2025	0.441	0.731	0.127	0.362
Tree	RB	1990	0.711	1.048	0.383	0.509
	RB	1995	0.536	1.081	0.241	0.537
	RB	2000	0.507	1.053	0.235	0.558
	RB	2005	0.657	1.132	0.334	0.56
	RB	2010	0.693	1.055	0.328	0.553
	RB	2015	0.632	0.955	0.277	0.503
	RB	2020	0.542	0.878	0.227	0.448
	RB	2025	0.482	0.731	0.201	0.362
	RB + WC	1990	0.981	1.048	0.494	0.509
	RB + WC	1995	0.983	1.081	0.503	0.537
	RB + WC	2000	1.097	1.053	0.589	0.558
	RB + WC	2005	1.241	1.132	0.605	0.56
	RB + WC	2010	0.928	1.055	0.423	0.553
	RB + WC	2015	0.838	0.955	0.417	0.503
	RB + WC	2020	0.986	0.878	0.515	0.448
	RB + WC	2025	1.01	0.731	0.496	0.362
	RB x WC	1990	0.795	1.048	0.428	0.509
	RB x WC	1995	0.719	1.081	0.371	0.537
	RB x WC	2000	0.697	1.053	0.37	0.558
	RB x WC	2005	0.841	1.132	0.451	0.56
	RB x WC	2010	0.84	1.055	0.458	0.553
	RB x WC	2015	0.673	0.955	0.352	0.503
	RB x WC	2020	0.589	0.878	0.299	0.448
	RB x WC	2025	0.522	0.731	0.217	0.362